

Contents

3	1 Calibrations and corrections	1
4	1.1 Electron corrections	1
5	1.1.1 Energy scale and resolution correction	1
6	1.1.2 Electron selection efficiency	5
7	1.1.3 SF uncertainties propagation	9
8	1.2 Muon corrections	16
9	1.2.1 Muon momentum calibration	16
10	1.2.2 Correction for charge-dependent momentum bias	17
11	1.2.3 Muon efficiency measurements	23
12	1.3 Hadronic recoil calibration	28
13	1.3.1 SET and u_T reweighting	29
14	1.3.2 u_X and u_Y correction	32
15	1.3.3 Resolution and response corrections	33
16	1.4 Angular coefficients correction	35
17	Bibliography	36

List of Figures

19	11 Schematic overview of energy response calibration procedure for electrons and photons. .	1
20	12 Energy scale factors α for low pile-up runs of 2017 (left), 2018 (right) and 2017 at 5TeV	
21	(bottom) using 68, 48 and 24 η bins. It can be seen, that the extraction is unstable in case of	
22	68 bins, resulting in α factors with very large uncertainties.	3

23	13	Additional constant term c'_i for low pile-up runs of 2017 (13 TeV), 2018 (13 TeV) and 2017	
24		at 5 TeV using 24 bins. The lower panel shows the difference of c'_i to the 2017 5 TeV run.	3
25	14	The invariant mass distribution around the Z-mass for low pile-up Data for 2017 (13 TeV)	4
26	15	The invariant mass distribution around the Z-mass for low-pileup data for the $\sqrt{s} = 5$ TeV	
27		data taken in 2017 (a) and the $\sqrt{s} = 13$ TeV 2018 data (b).	4
28	16	Comparison of the uncertainties due to electron reconstruction, contrasting the high- μ -	
29		extrapolated and in-situ-measured SF uncertainties in a $W^+ \rightarrow e^+ \nu$ selection at 13 TeV as	
30		function of typical kinematic variables.	7
31	17	Isolation $E_T^{\text{cone}0.3}/25$ GeV distribution of probe electrons in the ZIso-method using 13 TeV	
32		339pb^{-1} low-pileup data. Left the denominator and right the numerator distributions	
33		are shown, with the data as crosses, the signal $Z \rightarrow ee$ expectation as open line and the	
34		background estimate as cyan area (template normalised at high values).	8
35	18	Comparison of electron reconstruction SFs with 5 TeV and 13 TeV data as well as the 5+13	
36		TeV combination in nine η ranges as written in the plot legend, from most central $\eta = 0 - 0.1$	
37		(top left) to most forward $\eta = 2.37 - 2.47$ (bottom right). The bottom panel shows the ratio	
38		of 5 TeV and 13 TeV SFs. The total uncertainties are shown.	10
39	19	Electron isolation efficiencies (top panels) and scale factors (lower panels) for the $ptvar-$	
40		$cone20/p_T^e < 0.1$ working point using 13 TeV 339pb^{-1} low-pileup data as function of η in	
41		bins of p_T	11
42	110	Electron trigger efficiencies (top panels) and scale factors (lower panels) for HLT_e15_1h1oose_nod0_L1EM12	
43		using 13 TeV 339pb^{-1} low-pileup data as function of η in bins of p_T	12
44	111	Total relative uncertainties of electron scale factors at 13 TeV measured with tag-and-probe	
45		method	13
46	112	Contributions to the electron uncertainties related to efficiency SF (reconstruction, iden-	
47		tification, isolation and trigger) in a $W^+ \rightarrow e^+ \nu$ selection at 13 TeV as function of typical	
48		kinematic variables.	14
49	113	Contributions to the electron uncertainties related to efficiency SF (reconstruction, iden-	
50		tification, isolation and trigger) in a $W^+ \rightarrow e^+ \nu$ selection at 5 TeV as function of typical	
51		kinematic variables.	15
52	114	Example fits to $J/\psi \rightarrow \mu\mu$ (left) and $Z \rightarrow \mu\mu$ (right) mass peaks for pairs with leading muon	
53		pseudorapidity in the range $-0.62 < \eta < -0.52$ in low-pile-up 2017 13 TeV data.	16
54	115	Mean (left) and width (right) of the $J/\psi \rightarrow \mu\mu$ mass peak as a function of the leading	
55		muon η in 5.02 TeV data and MC. The mean and width are extracted from Crystal Ball	
56		components of the fits. In case of the simulation, both the uncorrected (dashed histogram)	
57		and corrected parameters (solid histogram) are shown. The fit results are presented for	
58		mass peaks constructed using kinematics of the muon ID tracks (top), ME tracks (mid-	
59		dle) or CB tracks (bottom). The bottom panels in each plot show the data/MC ratio for	
60		uncorrected (dashed histogram) and corrected simulation (points).	18

61	116	Mean (left) and width (right) of the $J/\psi \rightarrow \mu\mu$ mass peak as a function of the leading muon η in 2017 13 TeV data and MC at low pile-up. The mean and width are extracted from Crystal Ball components of the fits. In case of the simulation, both the uncorrected (dashed histogram) and corrected parameters (solid histogram) are shown. The fit results are presented for mass peaks constructed using kinematics of the muon ID tracks (top), ME tracks (middle) or CB tracks (bottom). The bottom panels in each plot show the data/MC ratio for uncorrected (dashed histogram) and corrected simulation (points).	19
68	117	Mean (left) and width (right) of the $Z \rightarrow \mu\mu$ mass peak as a function of the leading muon η in 5.02 TeV data and MC. The mean and width are extracted from Crystal Ball components of the fits. In case of the simulation, both the uncorrected (dashed histogram) and corrected parameters (solid histogram) are shown. The fit results are presented for mass peaks constructed using kinematics of the muon ID tracks (top), ME tracks (middle) or CB tracks (bottom). The bottom panels in each plot show the data/MC ratio for uncorrected (dashed histogram) and corrected simulation (points).	20
75	118	Mean (left) and width (right) of the $Z \rightarrow \mu\mu$ mass peak as a function of the leading muon η in 2017 13 TeV data and MC at low pile-up. The mean and width are extracted from Crystal Ball components of the fits. In case of the simulation, both the uncorrected (dashed histogram) and corrected parameters (solid histogram) are shown. The fit results are presented for mass peaks constructed using kinematics of the muon ID tracks (top), ME tracks (middle) or CB tracks (bottom). The bottom panels in each plot show the data/MC ratio for uncorrected (dashed histogram) and corrected simulation (points).	21
82	119	Sagitta bias corrections derived for 2017 low-pile-up data (left) and simulation (right) at $\sqrt{s} = 13$ TeV. The corrections are evaluated with two Z -mass methods (" $M_{\mu\mu_MCP}$ " and " $M_{\mu\mu_Align}$ "), the E/p method applied to $W \rightarrow e\nu$ (" $Wenv_E/p$ ") and $Z \rightarrow ee$ (" Zee_E/p ") events, and the $p_T(\mu)$ method, all of which are discussed in the text. The top plot shows the data results, where with clear η -dependent and overall biases are observed. The bottom plot shows MC, where a bias smaller by a factor of at least 10, with the exception of the electron E/p method.	22
89	120	Sagitta bias correction based on 2017 low-pile-up data at $\sqrt{s} = 13$ TeV. The statistical uncertainty (combined from uncertainties of the η -dependent correction and the global offset correction) is represented by error bars.	22
92	121	Comparison of reconstruction efficiencies for Medium muons using the low- μ runs of 2017 and 2018 at a centre-of-mass energy of $\sqrt{s} = 13$ TeV and $\sqrt{s} = 5$ TeV. Efficiencies are shown as a function of muon η, p_T . Red (orange) points correspond to low- μ data (MC), while the black (blue) points are high- μ data (MC). The bottom panels show the data/MC ratio for the low- μ (orange) and high- μ (blue) sets with statistical and total uncertainties.	24

97	122	Comparison of TTVA efficiencies for Medium muons using the low- μ runs of 2017+18 at $\sqrt{s} = 13$ TeV (top row) and low- μ runs of 2017 at $\sqrt{s} = 5$ TeV (lower row). The low- μ results compared to a high- μ data set as specified in the plot legend. Efficiencies are shown as function of muon η (left) and p_T (middle) and the mean number of interactions $\langle \mu \rangle$ (right). Red (orange) points correspond to low- μ data (MC), while the black (blue) points are high- μ data (MC). The bottom panels show the data/MC ratio for the low- μ (orange) and high- μ (blue) sets with statistical and total uncertainties.	25
104	123	1D trigger efficiency and systematic uncertainty in data and MC, 5 and 13 TeV from 2017 and 2018 for probes from the eta barrel region and inclusive ϕ , p_T distributions. Trigger sectors in the barrel and endcap regions are different, only the barrel trigger is shown here. The bin edges correspond to physical edges of the trigger sectors.	26
108	124	Efficiencies for Ptvarcone20 isolation selections measured in 2017 and 2018 data and MC 13 TeV and 5 TeV as a function of muon η (left) and p_T (right). The bottom panels show the data/MC scale factors with statistical uncertainties represented by blue boxes, while a sum in quadrature of statistical and systematic uncertainties is represented by orange boxes. . .	27
112	125	Hadronic recoil	29
113	126	Comparison of the $\Sigma E_T - p_T^{\ell\ell}$ description in data of the two MC samples POWHEG and SHERPA at 13 TeV, showing $\Sigma E_T - p_T^{\ell\ell}$ inclusively (left). Figure on the right shows the comparison of SHERPA to the data after a dedicated pileup reweighting.	30
116	127	Ratio of data to predictions in $W \rightarrow \mu\nu$ events at 13 TeV for the $\Sigma \vec{E}_T$ distribution, before and after each $\Sigma \vec{E}_T$ modeling reweighting step. The color band is the data statistical uncertainty. The prediction uncertainty only includes the statistical uncertainty. 'Powheg' uses the baseline MC for the signal. 'Powheg+Z2D' has the 2D $(\Sigma \vec{E}_T, p_T^{true,V})$, Z-based reweighting applied. 'Powheg+Z2D+SETUT' adds the $\Sigma \vec{E}_T$ reweighting in bins of u_T . 'Powheg+Z2D+SETUT+1DPT' adds the 1D reweighting to recover the initial $p_T^{true,V}$ spectrum.	31
122	128	Ratio of data to predictions in $W \rightarrow \mu\nu$ events at 5 TeV for the $\Sigma \vec{E}_T$ distribution, before and after each $\Sigma \vec{E}_T$ modeling reweighting step. The color band is the data statistical uncertainty. The prediction uncertainty only includes the statistical uncertainty. 'Powheg' uses the baseline MC for the signal. 'Powheg+Z2D' has the 2D $(\Sigma \vec{E}_T, p_T^{true,V})$, Z-based reweighting applied. 'Powheg+Z2D+SETUT' adds the $\Sigma \vec{E}_T$ reweighting in bins of u_T . 'Powheg+Z2D+SETUT+1DPT' adds the 1D reweighting to recover the initial $p_T^{true,V}$ spectrum.	32

128	129	$\phi(u_T)$ at 5 and 13 TeV, for the data and the simulation before and after u_X and u_Y correction,	
129		in Z events. The band in the ratio panel is the data statistical uncertainty.	34

130

List of Tables

131	11	Values of η_{calo} bin frontiers for energy scale factors for low pile-up runs.	2
-----	----	---	---

1 Calibrations and corrections

“Potentielle citation sans aucun rapport avec le sujet”

— Personne inconnue, contexte à déterminer

1.1 Electron corrections

This subsection describes the electron calibrations and corrections used in pTW analysis. They were derived from the low- μ special run data collected in 2017 and 2018 at 5 and 13 TeV and the dedicated Monte-Carlo (MC) samples [1], as well as from the standard ATLAS high pileup data collected during the Run 2.

1.1.1 Energy scale and resolution correction

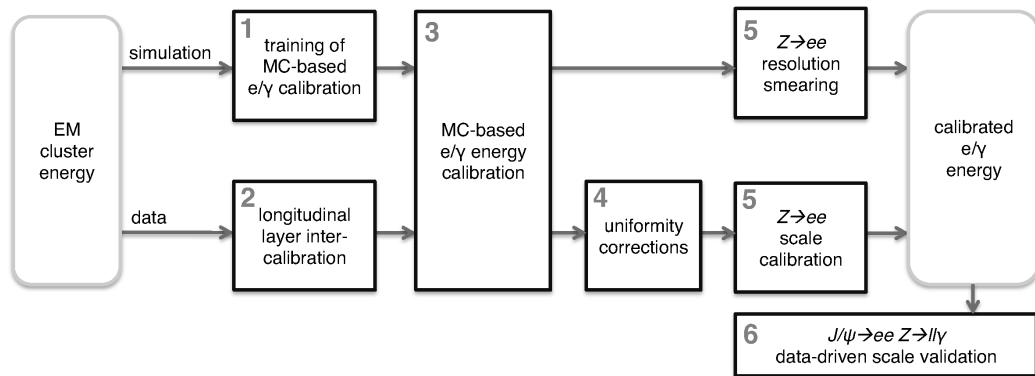


Figure 11: Schematic overview of energy response calibration procedure for electrons and photons.

In order to obtain the energy scale and resolution corrections the electrons from $Z \rightarrow ee$ process were used. The selection criteria were the same for data and MC simulation. For high- μ electron candidates must pass the triggers HLT_2e12_lhloose_L12EM10VH (2015), HLT_2e17_lhvloose_nod0 (2016), HLT_2e24_lhvloose_nod0 (2017) and HLT_2e24_lhvloose_nod0 (2018) [2]. In low pile-up case electron candidates must pass the triggers HLT_e15_lhloose_nod0_L1EM12. Both electrons are required to have $p_T > 27$ GeV and $|\eta| < 2.47$, satisfying the medium LH ID criteria and loose isolation criteria as described in Ref. [3]. Energy scale correction follows the method described in detail in

-2.47 -2.4 -2.1 -1.8 -1.55 -1.37 -1.2 -1 -0.8 -0.6 -0.4 -0.2 0 0.2 0.4 0.6 0.8 1 1.2 1.37 1.55 1.8 2.1 2.4 2.47

Table 11: Values of η_{calo} bin frontiers for energy scale factors for low pile-up runs.

[4] and schematically described in Fig. 11. The scale in both data and MC is calibrated using the MVA-based algorithm, then the data is corrected for pile-up and uniformity. The energy response in data is calibrated using the $Z \rightarrow ee$ peak to match exactly the Z resonance in the simulation. Two correction factors are introduced: the energy scale factor α and the constant term c' . The correction factors are extracted using the template method described in Ref. [5]:

- The calorimeter is split into i slices in η and for each slice the energy response in data is corrected in the following way:

$$E^{\text{data,corr}} = E^{\text{MC}} = E^{\text{data,uncorr}} / (1 + \alpha_i),$$

where $E^{\text{data,uncorr}}$ and E^{MC} are the energy response in data and MC respectively, α_i is the energy correction factor for the i^{th} calorimeter slice in η .

- The relative energy measurement resolution can be represented as a quadratic sum of three uncorrelated terms:

$$\frac{\sigma(E)}{E} = \frac{a}{\sqrt{E}} \oplus \frac{b}{E} \oplus c,$$

where b term stands for electromagnetic and pile-up noise term, a is the stochastic term related to the development of the electromagnetic shower and c is constant. In order to widen the MC mass peak and match it to the data in each rapidity bin an additional constant term c' is added:

$$\left(\frac{\sigma(E)}{E} \right)_i^{\text{data}} = \left(\frac{\sigma(E)}{E} \right)_i^{\text{MC}} \oplus c'_i.$$

Normally in the standard high-pileup data, the energy scale factors corrections are obtained in 68 η bins. For the low pile-up runs smaller bins were also considered due to smaller number of $Z \rightarrow ee$ events. Figure 12 demonstrates the need for wider bins, as 68 bins result in high uncertainty, especially in the endcap.

Two binnings were considered:

- 48 bins with smaller bins in the barrel and wider bins in the endcap
- 24 bins of equal size, as shown in Table 11.

As can be seen from Figure 12, the statistical instability for the endcap bins disappears if wider bins are used. Since the α factors are quite similar in 48 and 24 bin cases, the latter is chosen as the baseline.

The extracted constant c'_i correction term is presented in Figure 13. The constant term c' depends on the data taking conditions and pile-up, so its extrapolation from a dataset obtained under different conditions appears problematic. This issue is discussed in Ref. [6].

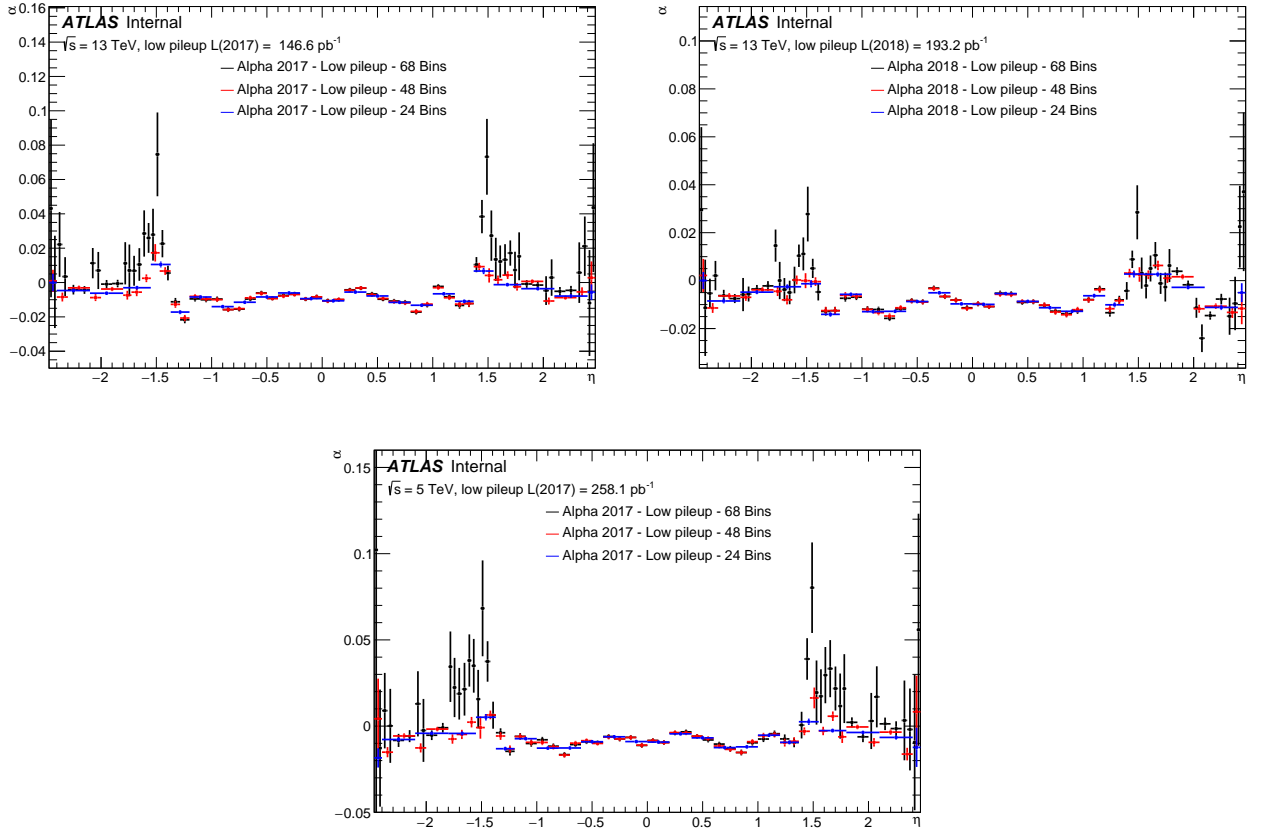


Figure 12: Energy scale factors α for low pile-up runs of 2017 (left), 2018 (right) and 2017 at 5TeV (bottom) using 68, 48 and 24 η bins. It can be seen, that the extraction is unstable in case of 68 bins, resulting in α factors with very large uncertainties.

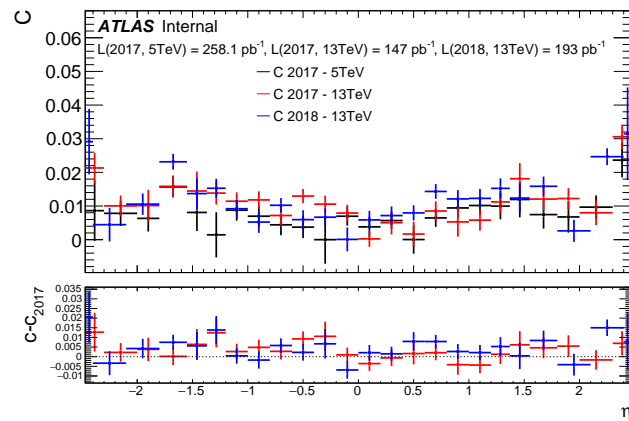


Figure 13: Additional constant term c'_i for low pile-up runs of 2017 (13 TeV), 2018 (13 TeV) and 2017 at 5 TeV using 24 bins. The lower panel shows the difference of c'_i to the 2017 5 TeV run.

168 This correction entails experimental uncertainty, caused primarily by the statistical uncertainty of
 169 α_i and c'_i factors measurement, other uncertainties are significantly smaller and therefore neglected.
 170 The comparison between data and MC invariant mass distributions around the $Z \rightarrow ee$ peak are
 171 presented in Figure 14 and Figure 15. The agreement is good around the $Z \rightarrow ee$ resonance and stays
 172 within the uncertainty in other regions.

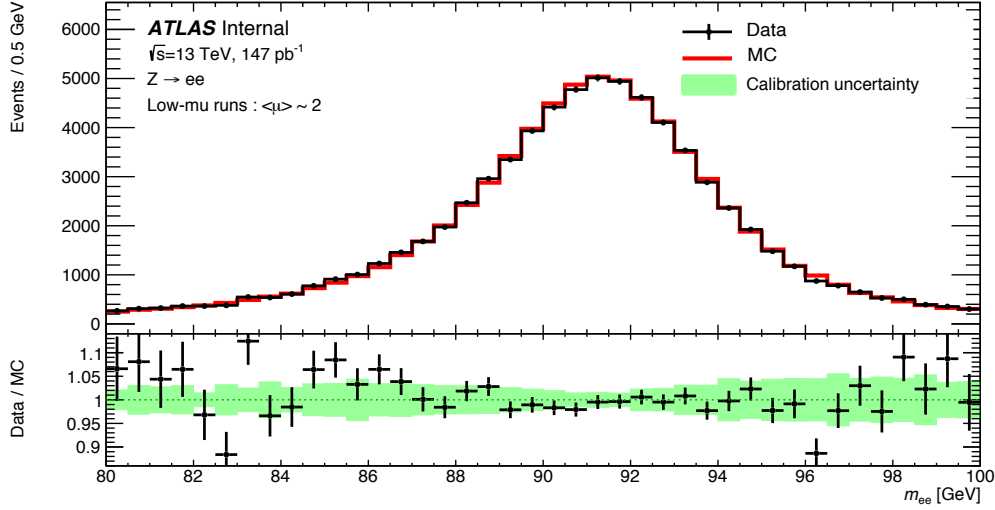


Figure 14: The invariant mass distribution around the Z-mass for low pile-up Data for 2017 (13 TeV)

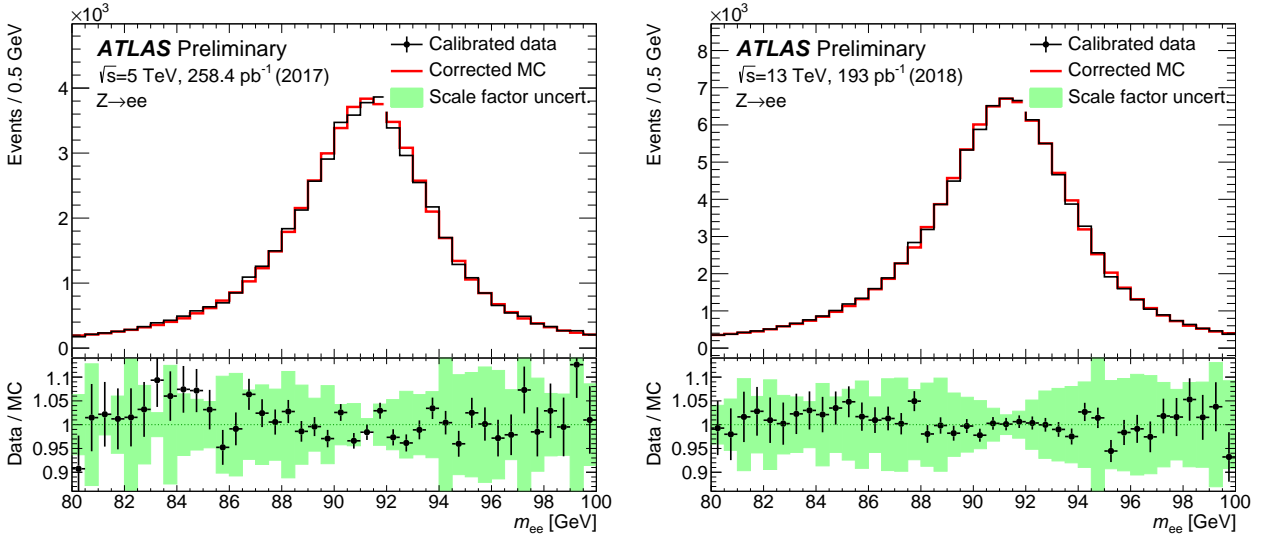


Figure 15: The invariant mass distribution around the Z-mass for low-pileup data for the $\sqrt{s} = 5$ TeV data taken in 2017 (a) and the $\sqrt{s} = 13$ TeV 2018 data (b).

1.1.2 Electron selection efficiency

The electrons used in the analysis are selected based on certain requirements to the quality of their reconstruction, kinematic characteristics, passing certain identification, isolation and trigger matching criteria. A tag-and-probe method is used to measure these efficiencies in data and MC simulation, which may be different due to various aspects of physics and detector modelling. In order to match the MC simulation and the data in each of the aforementioned aspects the corresponding scale factor (SF)s are introduced. The SF is defined as the ratio of the data efficiency to MC efficiency:

$$SF_{(a)} = \frac{\epsilon_{(a)}^{data}}{\epsilon_{(a)}^{MC}},$$

where ϵ stand for efficiency and index a stands for reconstruction, ID, isolation or trigger. The SF extraction allows for better comparison between data and simulation, but also brings uncertainties. The total efficiency correction is used as an event weight during the analysis:

$$W_{event}^{W \rightarrow e\nu} = SF_{reco} SF_{trig} SF_{ID} SF_{iso}.$$

The tag-and-probe method used for the measurement of electron efficiencies includes the following steps:

- A kinematic selection is applied to $Z \rightarrow ee$ events (Cut1).
- A tight selection (Cut2) is applied to one of the two electrons along with matching it to the single-electron trigger. From now on this electron is called the *tag*.
- The other electron is called the *probe* and is used to probe the picked efficiency.
- Selections Cut1 and Cut2 are varied in order to evaluate the uncertainties.

The details are presented in Refs. [2, 7, 8].

Reconstruction efficiency

The reconstruction efficiency is defined as a fraction of all electromagnetic clusters that are matched with the charged particle track from the Inner Detector (ID) that matches the designated quality criteria. An additional "PassTrackQuality" requirement of having at least 1 hit in the pixel detector and at least 7 hits in the silicon detectors is imposed on the track of successfully reconstructed electrons. So the electron reconstruction efficiency is calculated as:

$$\epsilon^{reco}(p_T, \eta) = \frac{N_{pass} - N_{pass}^{bkg}}{N_{pass} - N_{pass}^{bkg} + N_{fail} - N_{fail}^{bkg} + N_{photon} - N_{fit}}. \quad (1.1)$$

188 $N_{pass(fail)}$ stands for the number of electrons passing (failing) the "PassTrackQuality" criterion. The
 189 background electron candidates $N_{pass(fail)}^{bkg}$ are obtained from the template fits of the background on
 190 subsets that pass (fail) the "PassTrackQuality" criterion. The number of electrons that are reconstructed
 191 as photons is denoted by N_{photon} . The non-electron background that is reconstructed as photons is
 192 estimated from analytical fit in the control region away from the $Z \rightarrow ee$ resonance and is called N_{fit} .
 193 An extrapolation of SF_{reco} from the high- μ data is used as a baseline for the reconstruction scale factors
 194 measurement. The benefits of higher statistics available in high- μ dataset outweigh the losses imposed
 195 by the extrapolation and provide lower uncertainty comparing to the SFs measured with low pileup
 196 dataset (see Fig. 16).

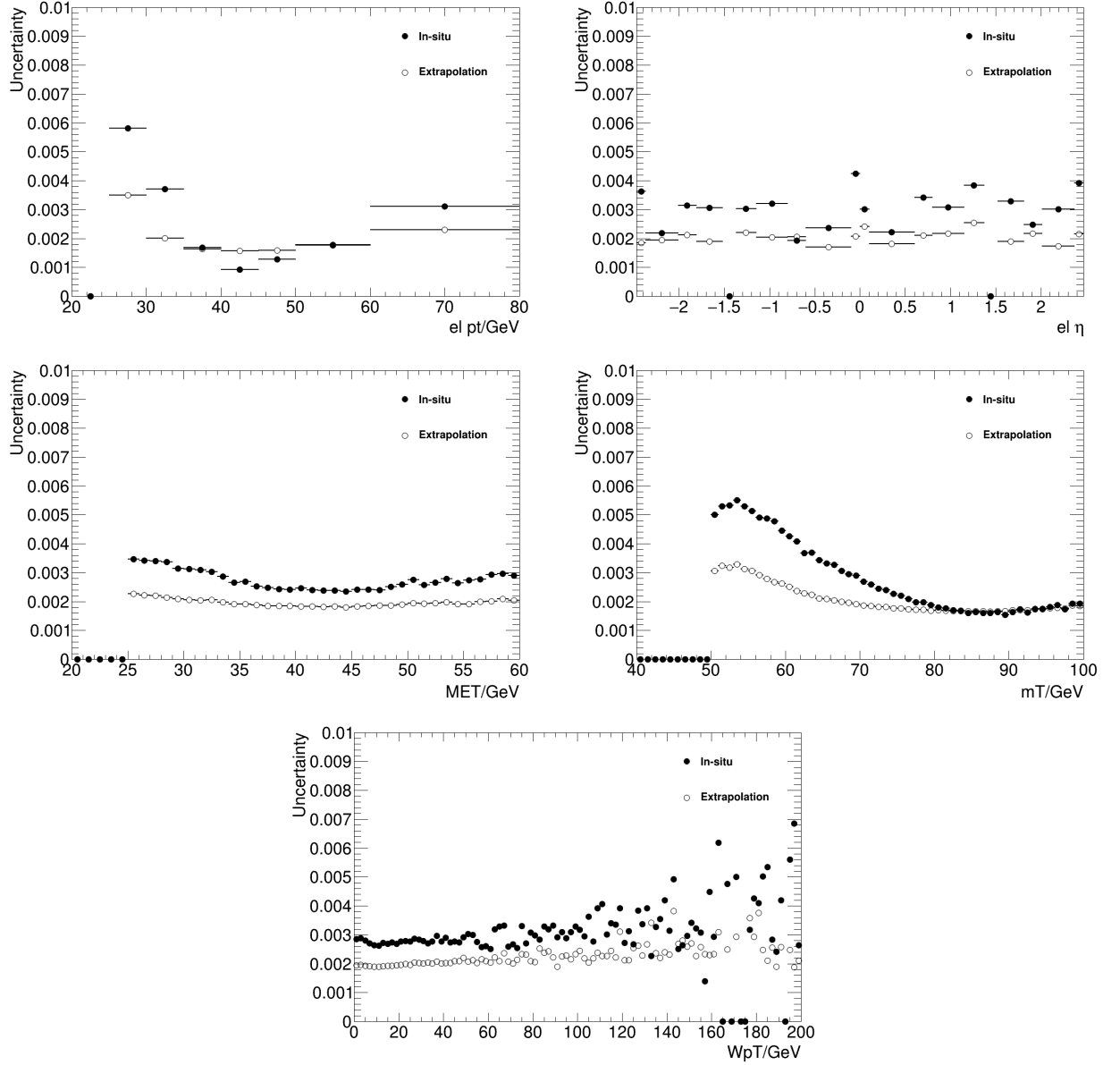


Figure 16: Comparison of the uncertainties due to electron reconstruction, contrasting the high- μ -extrapolated and in-situ-measured SF uncertainties in a $W^+ \rightarrow e^+ \nu$ selection at 13 TeV as function of typical kinematic variables.

197 Identification efficiency

198 The fraction of reconstructed electrons that pass a given working point define the electron identification
 199 efficiency. The low pile-up $W \rightarrow e\nu$ measurement uses "Medium LH" working point. The methodology
 200 is described in Ref. [7] and includes the combination of two background subtraction methods: Z_{mass}
 201 and Z_{iso} .

202 In the Z_{mass} method the background is estimated using a template method normalized in m_{ee} side
 203 bands. The tag is required to be trigger-matched, pass ID and isolation cuts and have $p_T > 20$ GeV. The
 204 probe has to pass the "PassTrackQuality" and the electron/photon ambiguity resolver, have $p_T > 15$
 205 GeV and be separated from jets with $p_T^{jet} > 20$ GeV by $\Delta R > 0.4$.

206 An alternative Z_{iso} method uses the calorimeter energy isolation E_T^{cone} of the probe electron to discrim-
 207 inate between background and signal. Signal electrons are expected to have better isolation than the
 208 background. On top of the requirements used for the Z_{mass} method the tag and probe pair is required
 209 to have opposite sign and to fit into mass window of 15 GeV around the Z boson mass. Background tem-
 210 plate shape is constructed from the probe electrons that have the same charge as the tag, pass the track
 211 quality criteria but fail the shower shape cuts or fail the cut-based loose identification. The fraction of
 212 real electrons that pass the described selection is modelled with MC and subtracted from the template.
 213 The background template uses the tail region of probe isolation distribution $E_T^{cone0.3}/25\text{GeV} > 0.5$ is
 214 scaled to data events. An example of the probe isolation estimate for the numerator and denominator
 215 in eq. 1.1 in the region $25 < E_T < 30$ and $0.8 < \eta < 1.15$ is presented in Fig. 17.

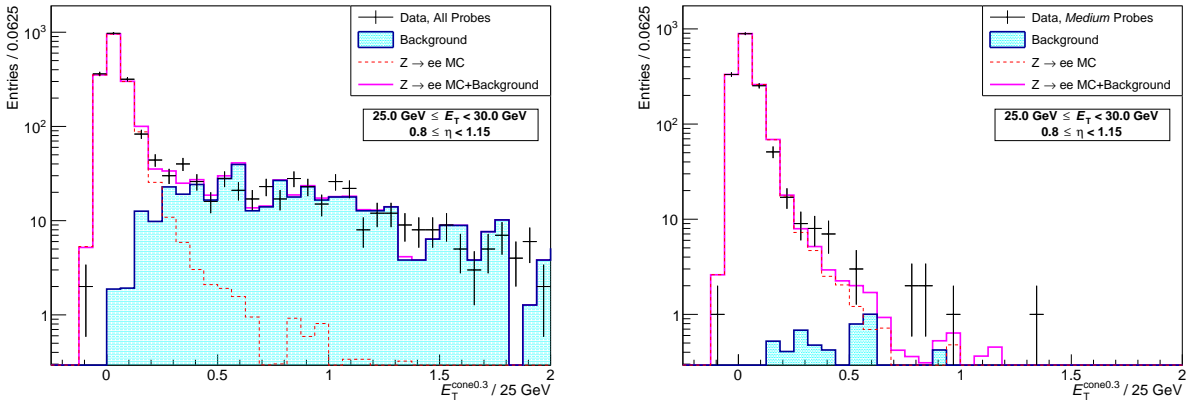


Figure 17: Isolation $E_T^{cone0.3}/25\text{GeV}$ distribution of probe electrons in the Z_{iso} -method using 13 TeV 339pb^{-1} low-pileup data. Left the denominator and right the numerator distributions are shown, with the data as crosses, the signal $Z \rightarrow ee$ expectation as open line and the background estimate as cyan area (template normalised at high values).

216 The SF to be used in the analysis is constructed out of both methods. The merger of the results takes
 217 into account the high degree of correlation of the two methods and includes the following steps:

- 218 • the final SF is defined as an arithmetic mean of the two methods over all systematic variations;

- the statistical uncertainty is calculated as an average of the statistical uncertainties of the variations;
- a covariance matrix is composed from all variations of the two methods and then decomposed into correlated and uncorrelated parts, providing the systematic uncertainty.

The combined results are presented in Fig. 18 and show similar results between both methods and the combination. The SFs obtained from 5 and 13 TeV data samples were not combined due to significant difference in measured efficiency.

Isolation efficiency

Electron isolation efficiency is a fraction of reconstructed and MediumLLH-identified electrons that pass a designated isolation requirement. For this analysis the isolation requirement is chosen to be $ptvarcone^{20}/p_T^e < 0.1$. The results are presented in Fig. 19 and show that the efficiency is very high. The SFs for 5 and 13 TeV are not combined and used separately.

Trigger efficiency

During the data-taking at low pile-up the unprescaled trigger HLT_e15_1h1oose_nod0_L1EM12 was used. Thanks to the ID and isolation requirements to both tad and probe, the background is negligible for trigger efficiency measurement. Measurement results are shown in Fig. 110 and demonstrate relatively high efficiency in most of the regions. The scale factors are also very close to unity. No combination was performed between 5 and 13 TeV results.

1.1.3 SF uncertainties propagation

The main source of uncertainty for the measurement of the SFs is coming from the background. The uncertainties are estimated by varying the parameters that contribute to background suppression. These parameters include:

- The Zmass window technique is used by identification, isolation and trigger efficiencies measurement. The size of the Zmass window was varied in a range of 10, 15 and 20 GeV. This variation dominates at higher values of p_T .
- Tag identification and isolation criteria were varied between Medium ID + calorimeter isolation, TightLLH and Tight ID + calorimeter isolation.
- Background template has a major influence on the estimate of signal contamination, especially at $p_T < 30$ GeV. In addition to the nominal range of template extraction in $120 < m_{ee} < 250$ the templates are also normalized using the region of $60 < m_{ee} < 70$ GeV.

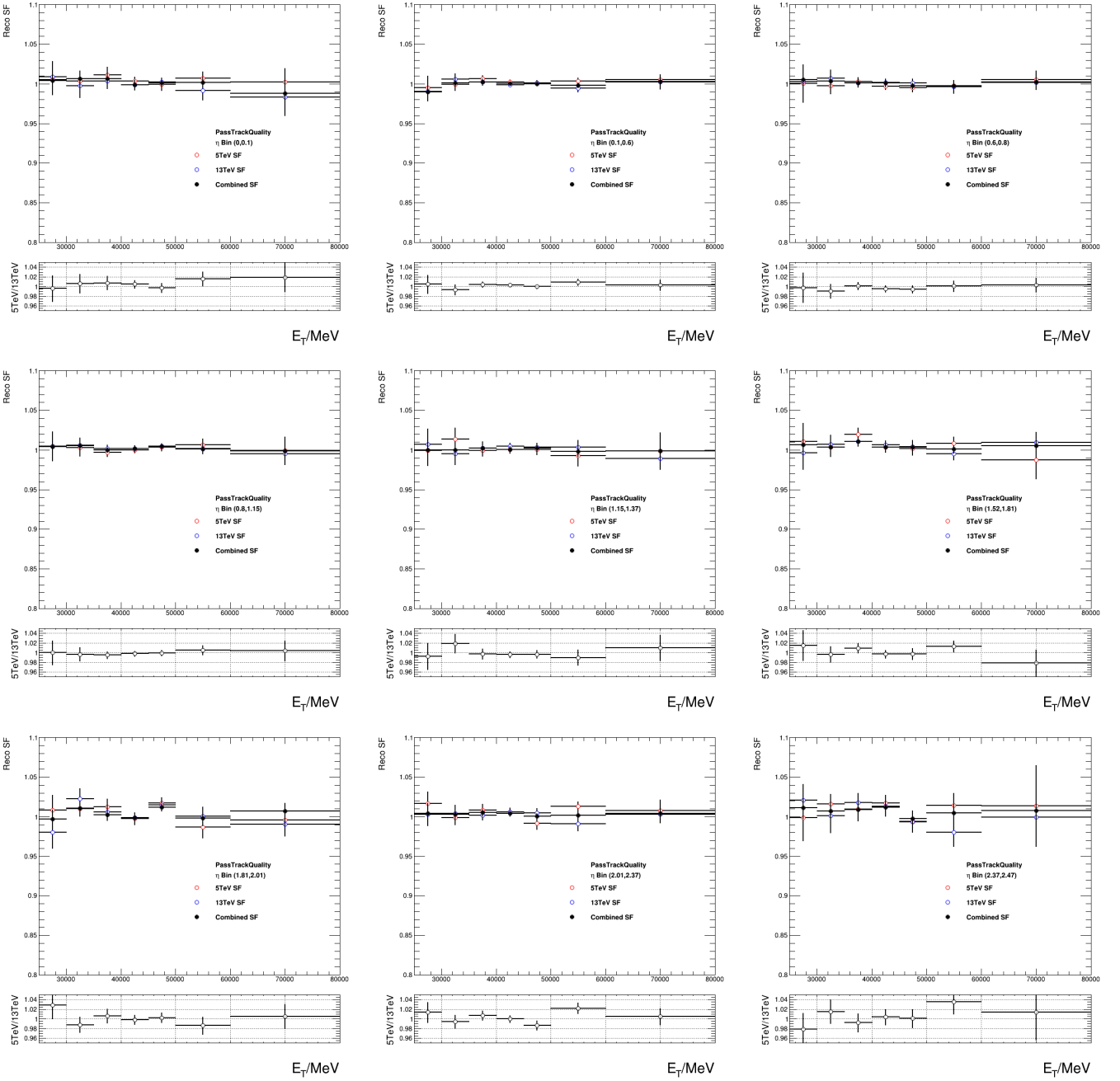
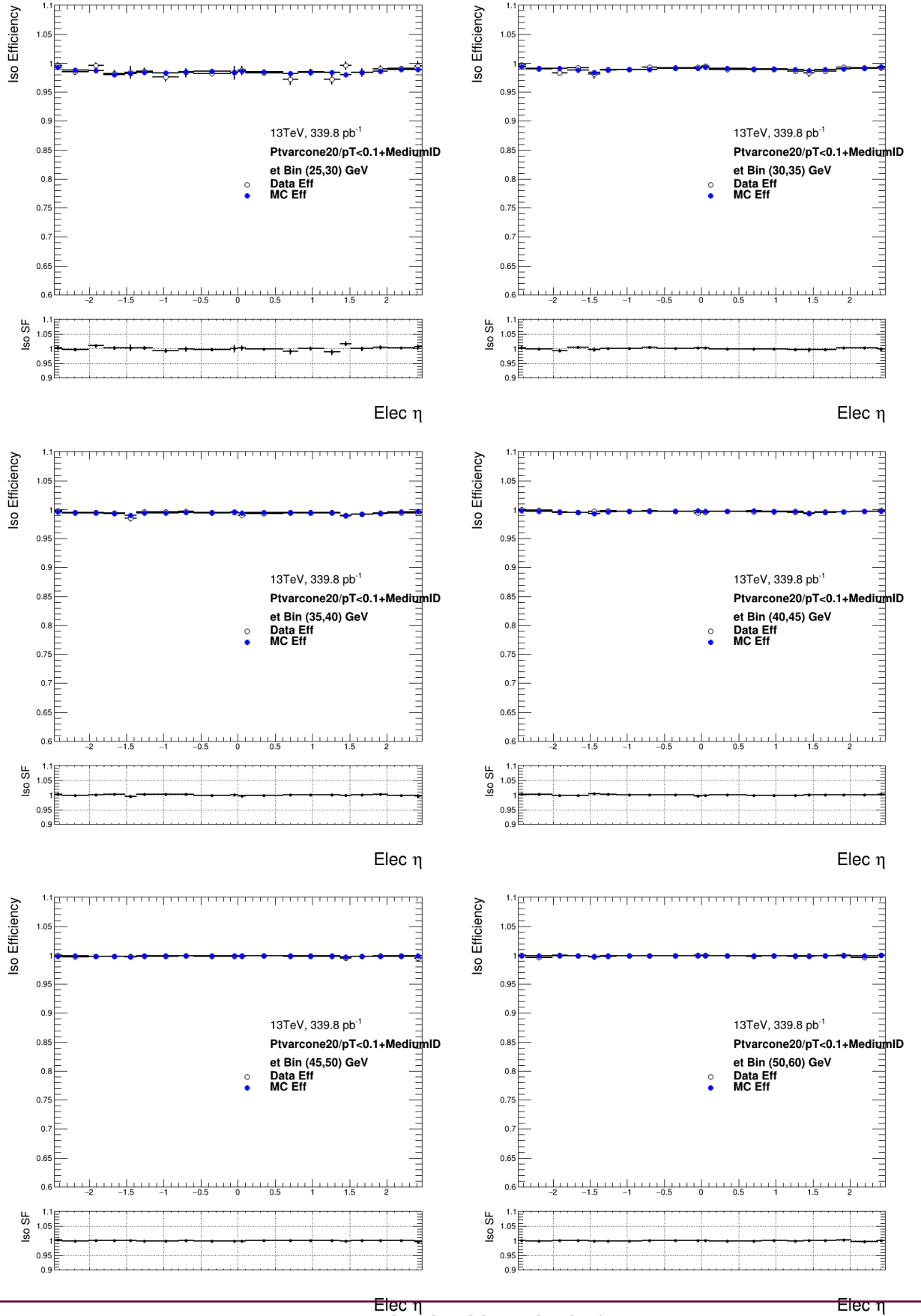


Figure 18: Comparison of electron reconstruction SFs with 5 TeV and 13 TeV data as well as the 5+13 TeV combination in nine η ranges as written in the plot legend, from most central $\eta = 0 - 0.1$ (top left) to most forward $\eta = 2.37 - 2.47$ (bottom right). The bottom panel shows the ratio of 5 TeV and 13 TeV SFs. The total uncertainties are shown.



1.1. ELECTRON CORRECTIONS

11

Figure 19: Electron isolation efficiencies (top panels) and scale factors (lower panels) for the $ptvarcone20/p_T^e < 0.1$ working point using 13 TeV 339 pb^{-1} low-pileup data as function of η in bins of p_T .

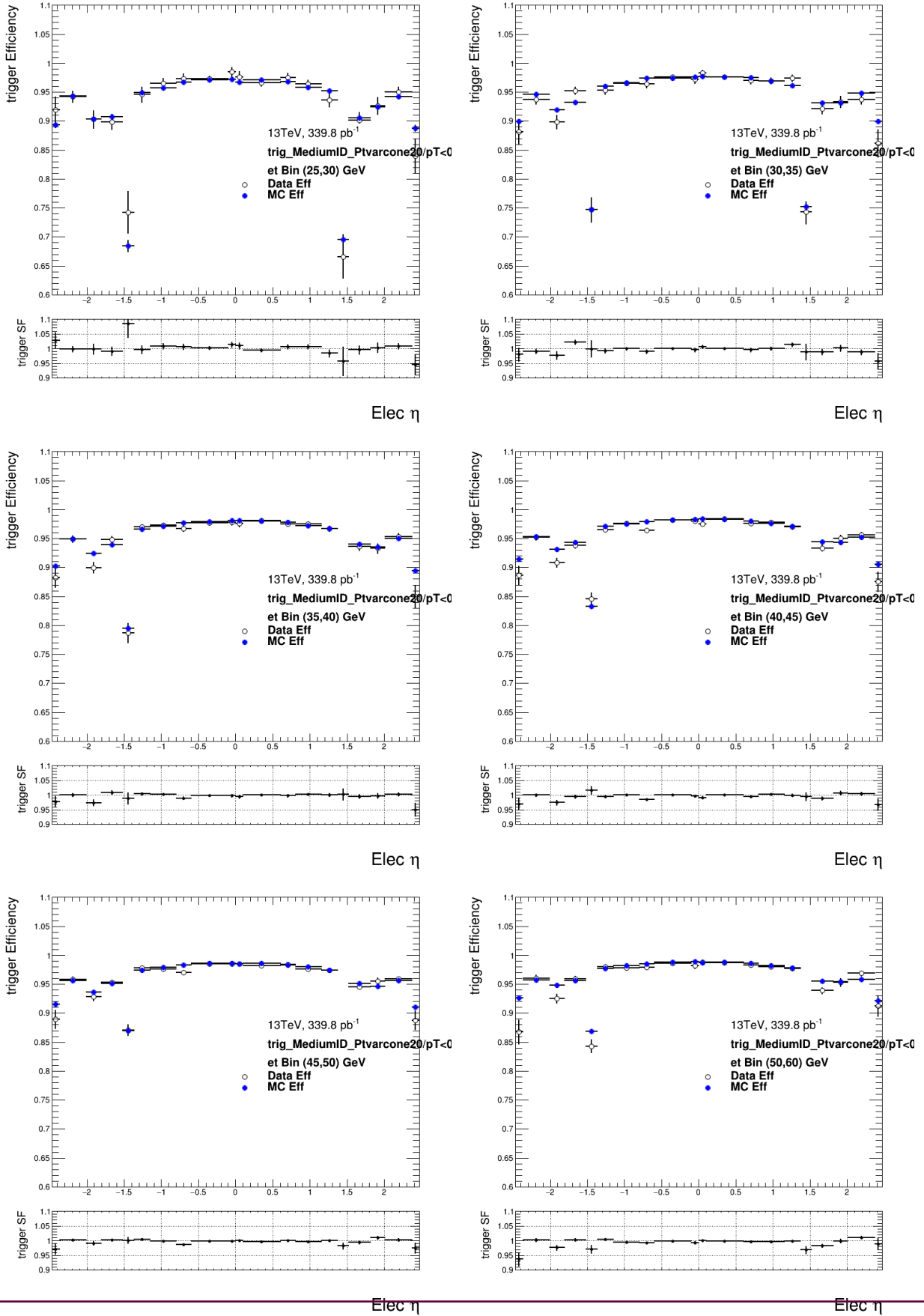


Figure 110: Electron trigger efficiencies (top panels) and scale factors (lower panels) for HLT_e15_1h1oose_nod0_L1EM12 using 13 TeV 339 pb⁻¹ low-pileup data as function of η in bins of p_T .

- Side band range is varied for reconstruction efficiency measurement.
- Isolation criteria are varied in the measurement of ID efficiency: $E_T^{cone0.3}/25\text{GeV}$ is varied between 0.4, 0.5 and 0.6, also a larger cone isolation around the probe electron was used - $E_T^{cone0.4}/25\text{GeV}$.

Figure 111 shows the total relative uncertainties of the electron scale factors at 13 TeV in different η bins. Contributions from reconstruction and identification are the dominant ones. The uncertainties are propagated to the observables using the co-called Full correlation model (see Ref. [8]). The idea of the method is to split the sources of SF uncertainty into uncorrelated and correlated sources. Uncorrelated sources are of statistical nature and mostly related to the number of $Z \rightarrow ee$ pairs in different bins if p_T and η used for SF extraction. Correlated sources of systematic uncertainty arise from the flaws of background subtraction. In the Full correlation model includes about 10 sources of systematic uncertainty and around 200 $p_T \times \eta$ bins as sources of statistical uncertainty and allows to propagate these uncertainties to the observables. Figures 112 and 113 contain the results of error propagation for 13 and 5 TeV respectively. Again, identification and reconstruction uncertainties have the largest contribution to the total SF uncertainty.

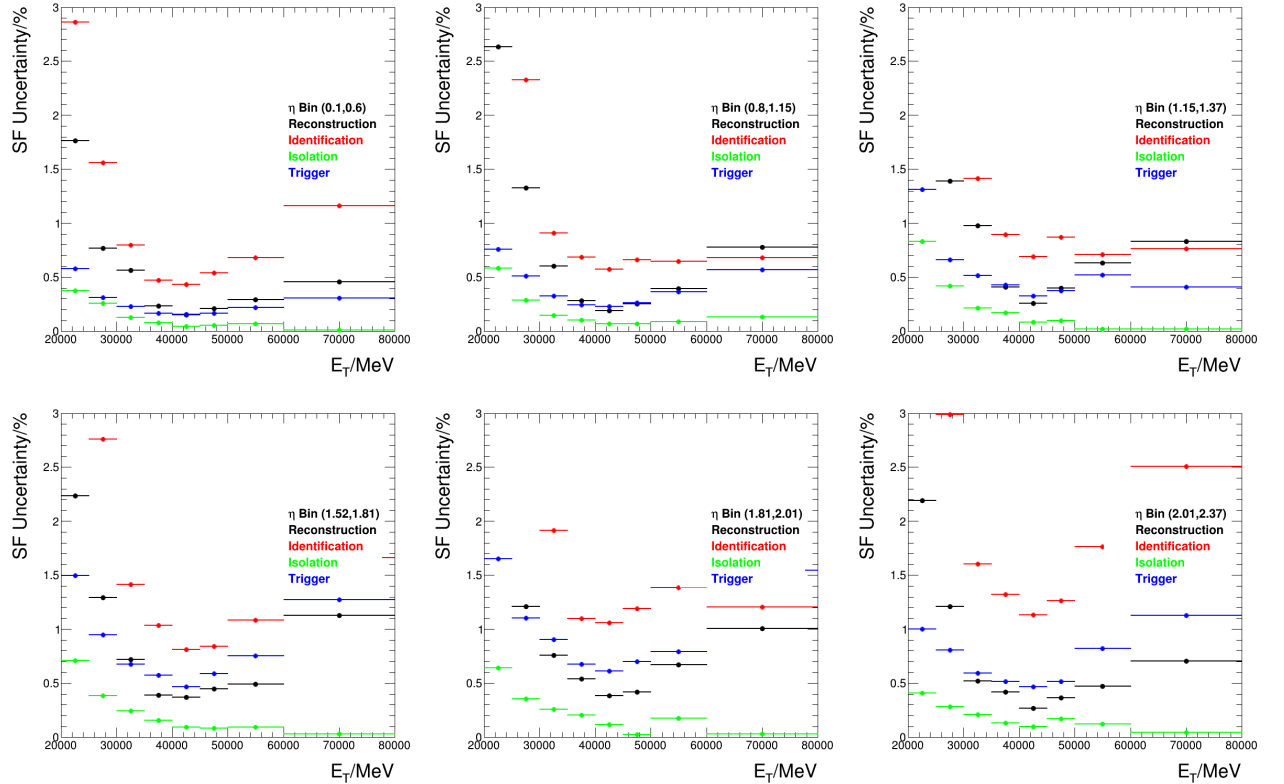


Figure 111: Total relative uncertainties of electron scale factors at 13 TeV measured with tag-and-probe method

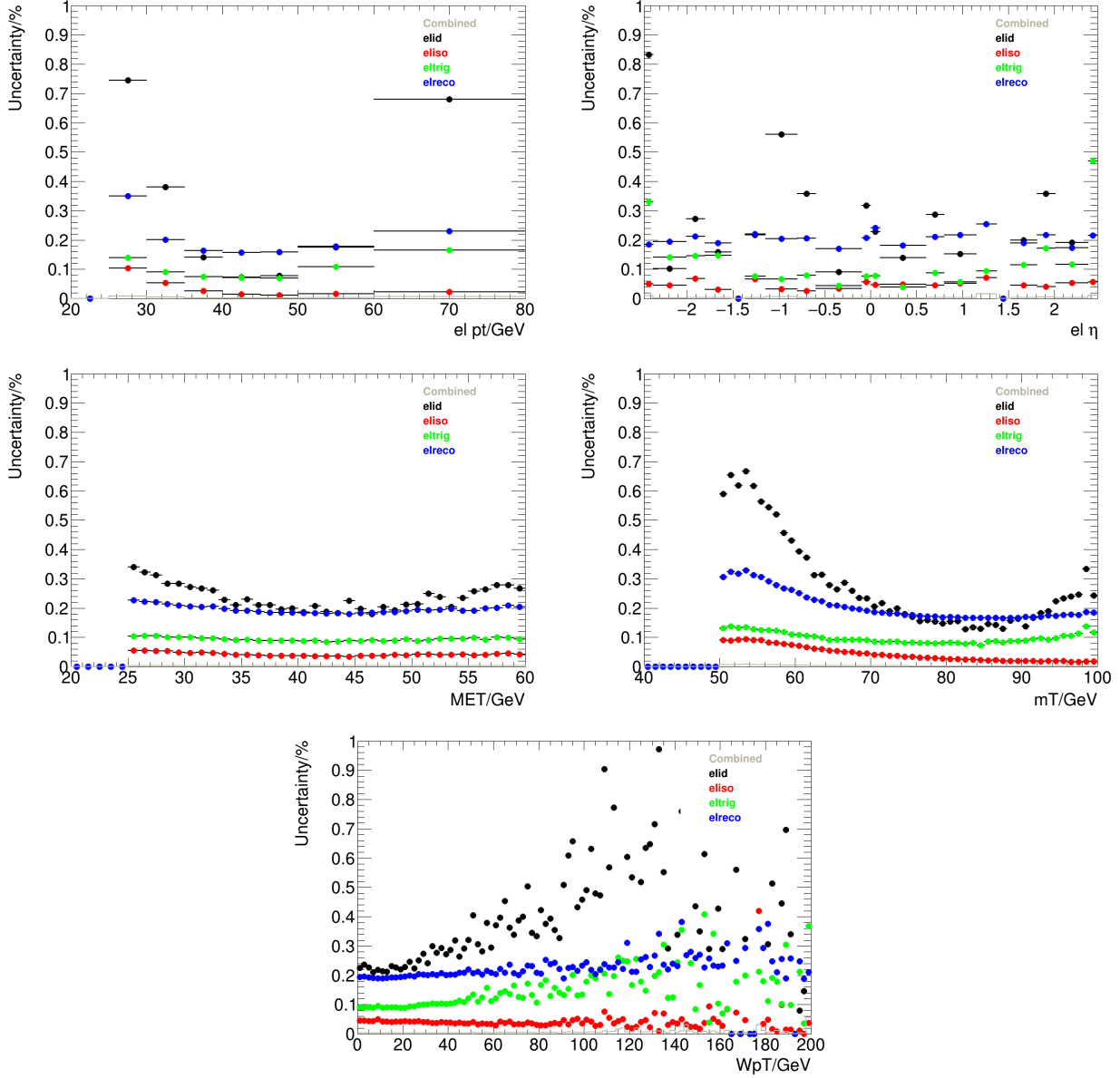


Figure 112: Contributions to the electron uncertainties related to efficiency SF (reconstruction, identification, isolation and trigger) in a $W^+ \rightarrow e^+ \nu$ selection at 13 TeV as function of typical kinematic variables.

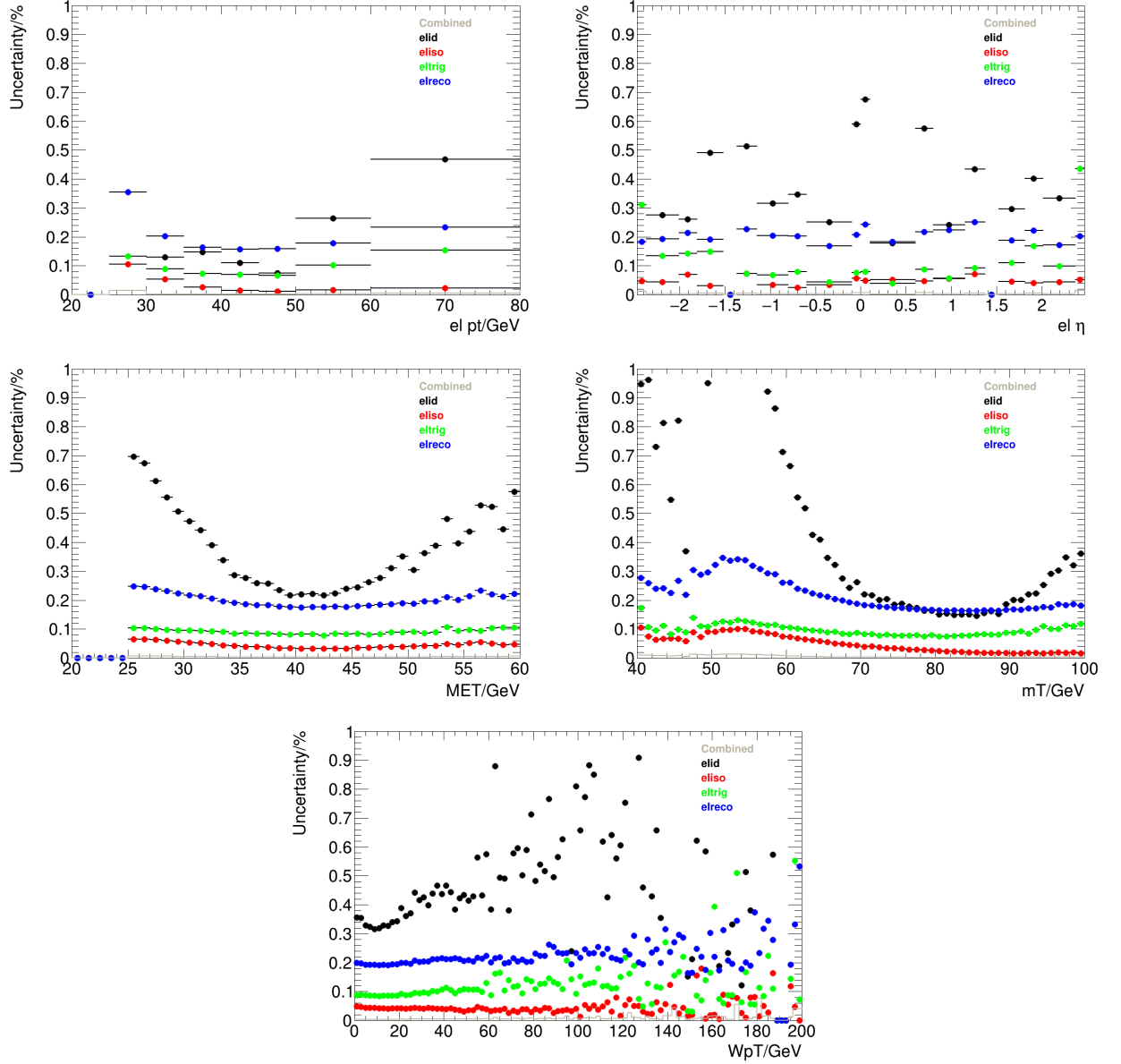


Figure 113: Contributions to the electron uncertainties related to efficiency SF (reconstruction, identification, isolation and trigger) in a $W^+ \rightarrow e^+ \nu$ selection at 5 TeV as function of typical kinematic variables.

1.2 Muon corrections

Muon corrections are in many aspects similar to the electron corrections described in the previous section. Calibrations are used in order to match the data and MC simulation

1.2.1 Muon momentum calibration

The muon momentum calibration comprises corrections to the momentum scale and resolution. At first the ID and Muon Spectrometer (MS) tracks are reconstructed and corrected separately, and then the two corrections are propagated to correct the CB muon tracks. Low energy muons with $5 < p_T < 30$ GeV are calibrated using the $J/\psi \rightarrow \mu\mu$ resonance, while in higher energy region of $22 < p_T < 300$ GeV the $Z \rightarrow \mu\mu$ resonance is used. The statistical uncertainties are directly linked to the number of Z and J/ψ candidates in the data samples:

- 5.02 TeV data (2017, period M): 660k J/ψ candidates, 75k Z candidates
- 13 TeV data (2017, period N): 1.1M J/ψ candidates, 100k Z candidates
- 13 TeV data (2018, periods G4 and J): 1.5M J/ψ candidates, 130k Z candidates

The Z and J/ψ peaks are fitted with a function that is a sum of a Crystal Ball function (that fits the mass peak), a Gaussian (that accounts for effects like multiple scattering) and an exponential that fits the backgrounds. The examples of such fits are presented at Fig. 114.

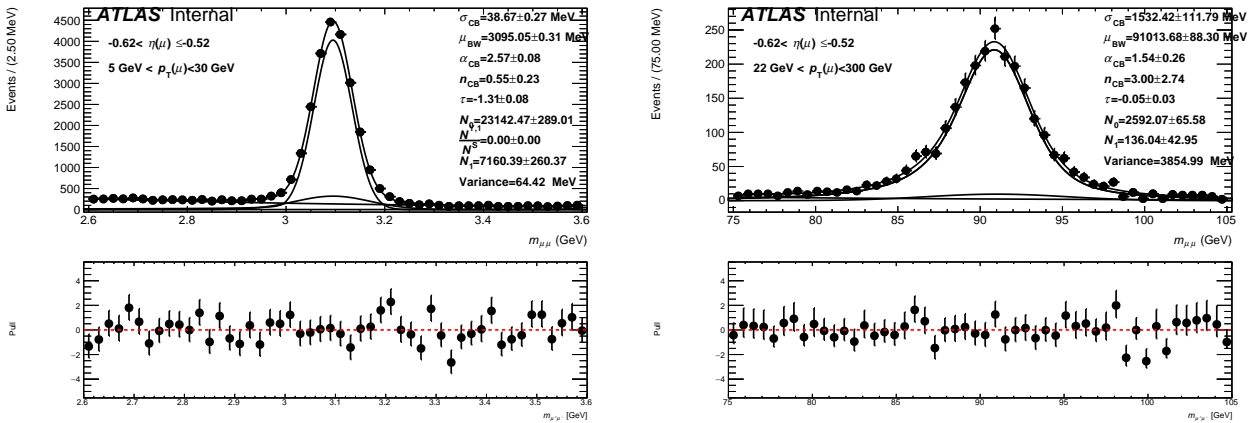


Figure 114: Example fits to $J/\psi \rightarrow \mu\mu$ (left) and $Z \rightarrow \mu\mu$ (right) mass peaks for pairs with leading muon pseudorapidity in the range $-0.62 < \eta < -0.52$ in low-pile-up 2017 13 TeV data.

The measured correction parameters for Z and J/ψ peaks for 5 and 13 TeV are presented in Figures 115, 116, 117 and 118.

1.2.2 Correction for charge-dependent momentum bias

Misalignment in ID, MS or between the two systems can lead to a charge-dependent bias (also called *sagitta bias*) of muon reconstructed momentum. Its effect can be parametrized as follows:

$$p_T^{meas} = \frac{p_T^{reco}}{1 + q\delta_{sagitta}}, \quad (1.2)$$

where p_T^{meas} is the measured momentum that contains a bias, p_T^{reco} is the unbiased reconstructed momentum and the bias to be corrected is denoted as $\delta_{sagitta}$.

The sagitta correction is obtained as a function of η . There exist three methods of sagitta bias determination:

- The ID alignment and momentum measurement can be tested with electrons which have additional information from the charge-independent calorimeter. Using $Z \rightarrow ee$ and/or $W \rightarrow e\nu$ events it is possible to determine the charge bias of an electron track:

$$\delta_{sagitta} = \frac{\langle E/p_{track} \rangle^+ - \langle E/p_{track} \rangle^-}{2 \langle p_T^{calo} \rangle}, \quad (1.3)$$

where p_{track} is the momentum measured in the ID, E is the energy measured in the electromagnetic calorimeter (EMC), from which we can get the $p_T^{calo} = E \sin \theta$ transverse momentum. The $\langle \rangle$ brackets denote the averaging in η bins.

- The $p_T(\mu)$ method is used by muon combined performance (MCP) and alignment groups in high- μ data compares the muons and anti-muons spectra in $Z \rightarrow \mu\mu$ events.
- The Z-mass method uses the Z mass peak. This is the main method used by MCP and alignment groups, the results are denoted as $M_{\mu\mu_MCP}$ and $M_{\mu\mu_Align}$ on the plots (see [9]). The sagitta bias is calculated iteratively minimizing the difference between the reconstructed and expected position of the $Z \rightarrow \mu\mu$ mass peak position.

The results of these methods are presented in Fig. 119. The sagitta bias in low-pile-up data was found to be 10 times higher than in the MC simulation. Further results in the measurement rely on the following method: the differences between the data and MC are averaged over η using a fit, and also introduce a global offset. The results are shown in Fig. 120.

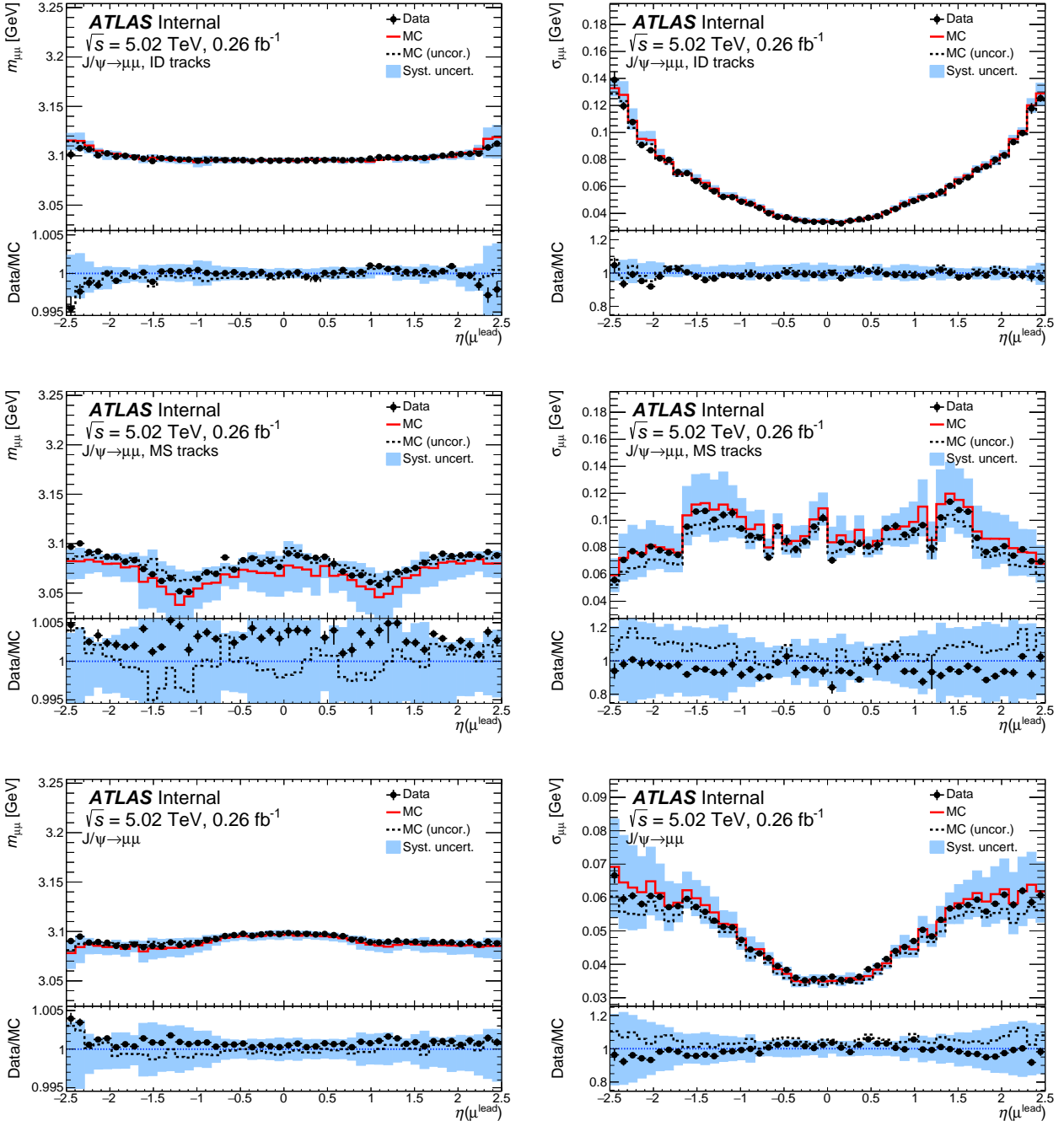


Figure 115: Mean (left) and width (right) of the $J/\psi \rightarrow \mu\mu$ mass peak as a function of the leading muon η in 5.02 TeV data and MC. The mean and width are extracted from Crystal Ball components of the fits. In case of the simulation, both the uncorrected (dashed histogram) and corrected parameters (solid histogram) are shown. The fit results are presented for mass peaks constructed using kinematics of the muon ID tracks (top), ME tracks (middle) or CB tracks (bottom). The bottom panels in each plot show the data/MC ratio for uncorrected (dashed histogram) and corrected simulation (points).

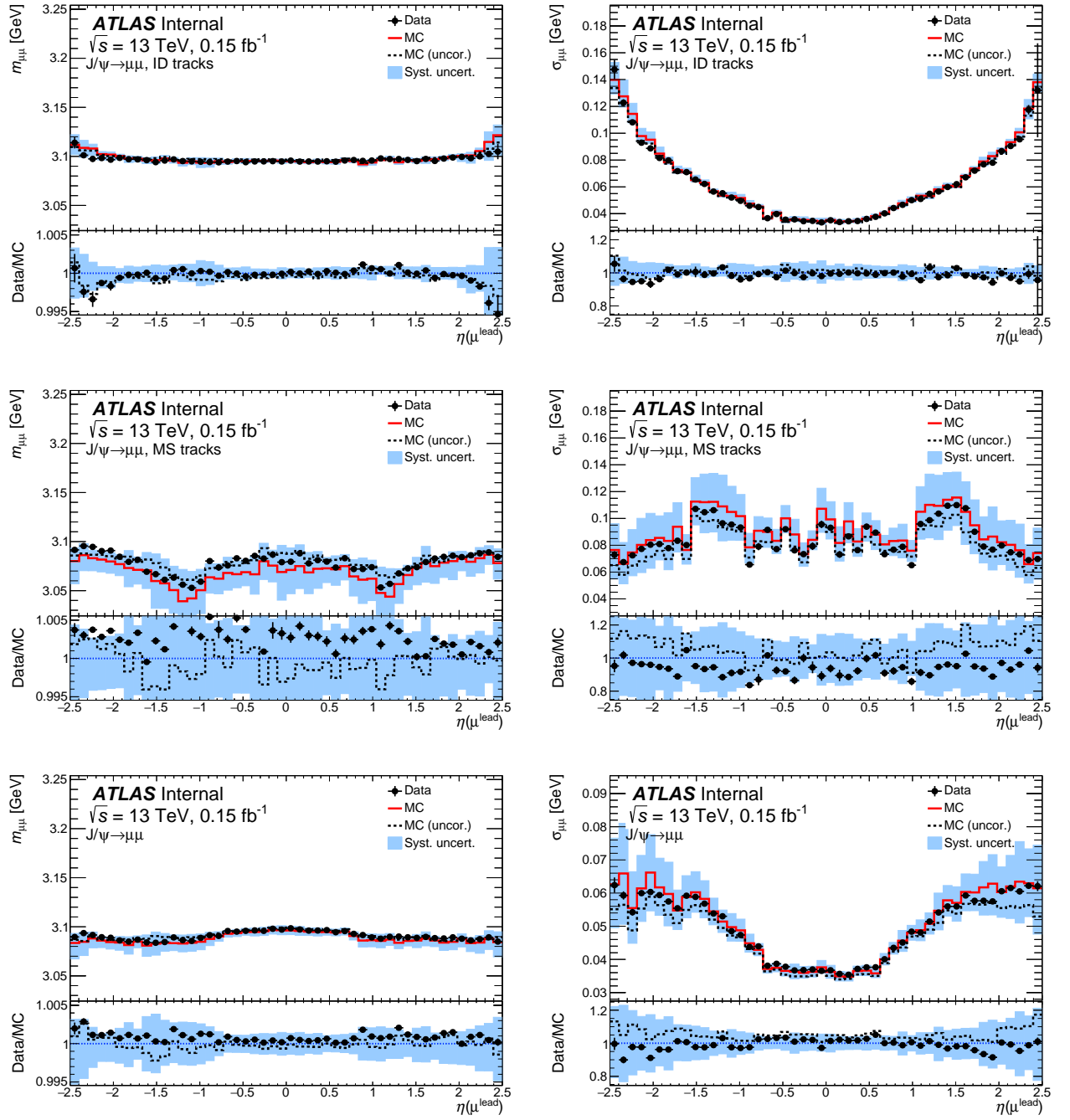


Figure 116: Mean (left) and width (right) of the $J/\psi \rightarrow \mu\mu$ mass peak as a function of the leading muon η in 2017 13 TeV data and MC at low pile-up. The mean and width are extracted from Crystal Ball components of the fits. In case of the simulation, both the uncorrected (dashed histogram) and corrected parameters (solid histogram) are shown. The fit results are presented for mass peaks constructed using kinematics of the muon ID tracks (top), ME tracks (middle) or CB tracks (bottom). The bottom panels in each plot show the data/MC ratio for uncorrected (dashed histogram) and corrected simulation (points).

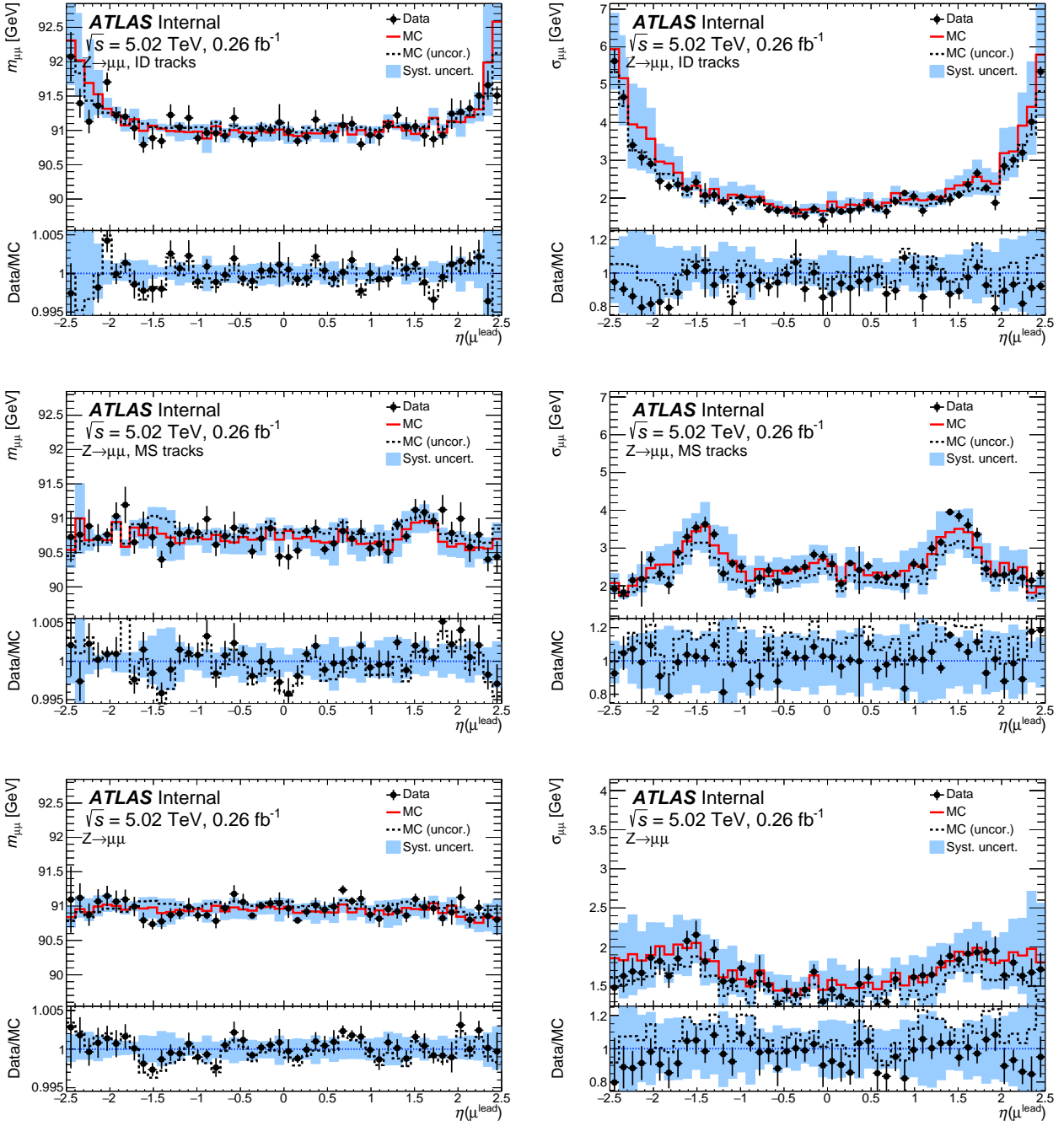


Figure 117: Mean (left) and width (right) of the $Z \rightarrow \mu\mu$ mass peak as a function of the leading muon η in 5.02 TeV data and MC. The mean and width are extracted from Crystal Ball components of the fits. In case of the simulation, both the uncorrected (dashed histogram) and corrected parameters (solid histogram) are shown. The fit results are presented for mass peaks constructed using kinematics of the muon ID tracks (top), ME tracks (middle) or CB tracks (bottom). The bottom panels in each plot show the data/MC ratio for uncorrected (dashed histogram) and corrected simulation (points).

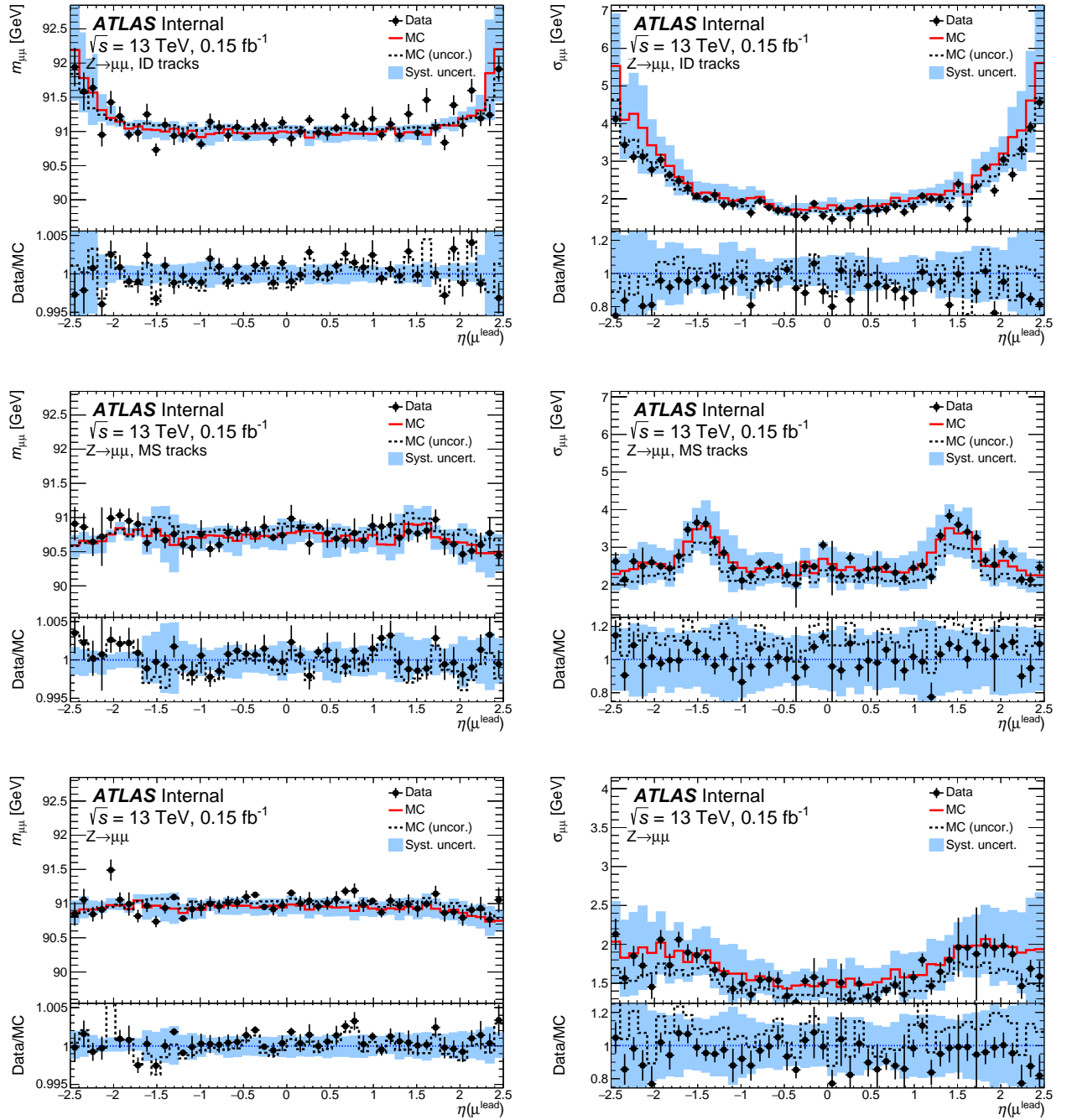


Figure 118: Mean (left) and width (right) of the $Z \rightarrow \mu\mu$ mass peak as a function of the leading muon η in 2017 13 TeV data and MC at low pile-up. The mean and width are extracted from Crystal Ball components of the fits. In case of the simulation, both the uncorrected (dashed histogram) and corrected parameters (solid histogram) are shown. The fit results are presented for mass peaks constructed using kinematics of the muon ID tracks (top), ME tracks (middle) or CB tracks (bottom). The bottom panels in each plot show the data/MC ratio for uncorrected (dashed histogram) and corrected simulation (points).

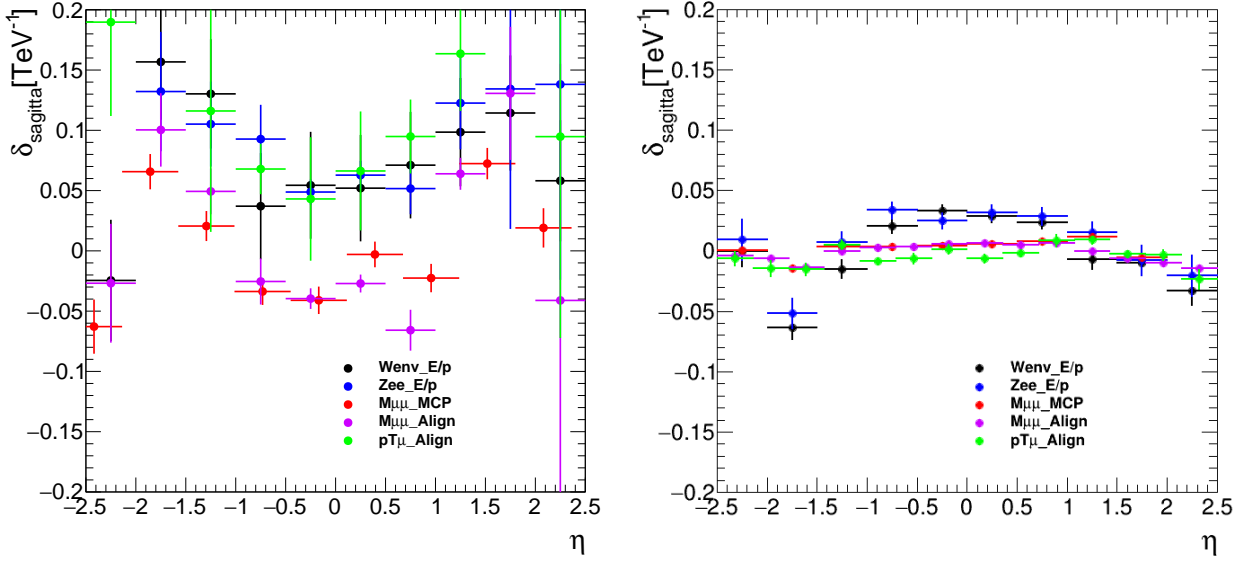


Figure 119: Sagitta bias corrections derived for 2017 low-pile-up data (left) and simulation (right) at $\sqrt{s} = 13$ TeV. The corrections are evaluated with two Z -mass methods (“ $M_{\mu\mu_MCP}$ ” and “ $M_{\mu\mu_Align}$ ”), the E/p method applied to $W \rightarrow e\nu$ (“ $Wenv_E/p$ ”) and $Z \rightarrow ee$ (“ Zee_E/p ”) events, and the $p_T(\mu)$ method, all of which are discussed in the text. The top plot shows the data results, where with clear η -dependent and overall biases are observed. The bottom plot shows MC, where a bias smaller by a factor of at least 10, with the exception of the electron E/p method.

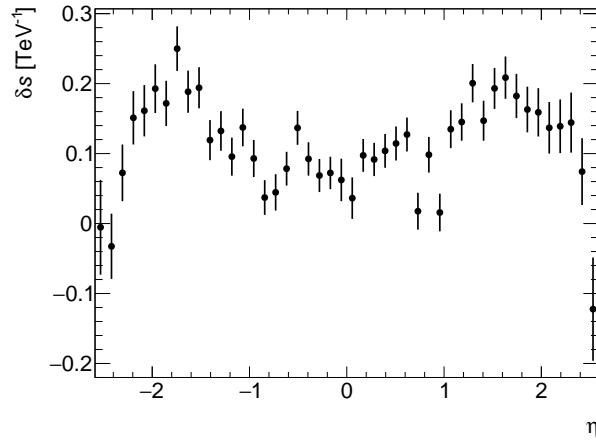


Figure 120: Sagitta bias correction based on 2017 low-pile-up data at $\sqrt{s} = 13$ TeV. The statistical uncertainty (combined from uncertainties of the η -dependent correction and the global offset correction) is represented by error bars.

1.2.3 Muon efficiency measurements

Just like in the case of electrons, muons have to pass a number of quality criteria in order to be used in the analysis:

- Reconstruction and identification: the muon is successfully reconstructed and its ID and MS tracks as well as EMC deposit are matched. The *medium* identification criterion is adopted for the low- μ analysis. Only CB and ME muons with loose requirements between the tracks from ID and MS are used. The value of q/p significance is required to be < 7 .
- Isolation: *LowMuWZPtvarcone20* selection was used, it has the track isolation requirement of $p_T^{varcone20}/p_T < 0.1$.
- Trigger: the muons were required to pass the *HLT_mu14* trigger.
- Track-to-vertex association (TTVA) includes requirement for the muon track to match the primary vertex. The muon objects are required to pass $|z_0|\sin\theta < 0.5$ mm and $d_0/\sigma(d_0) < 3$ requirements.

Just like in the case of electrons, possible discrepancies between the data and MC are corrected using the scale factors, which are in turn measured using the tag-and-probe method described in [10]. The product of the scale factors define the event weight:

$$W_{event}^{W \rightarrow e\nu} = SF_{reco/ID} \dot{S}F_{trig} \dot{S}F_{TTVA} \dot{S}F_{iso}.$$

All muon efficiencies and scale factors used in current analysis are measured in-situ using the low- μ datasets at 5 and 13 TeV by the MCP group. The results for their measurements are presented in Figures

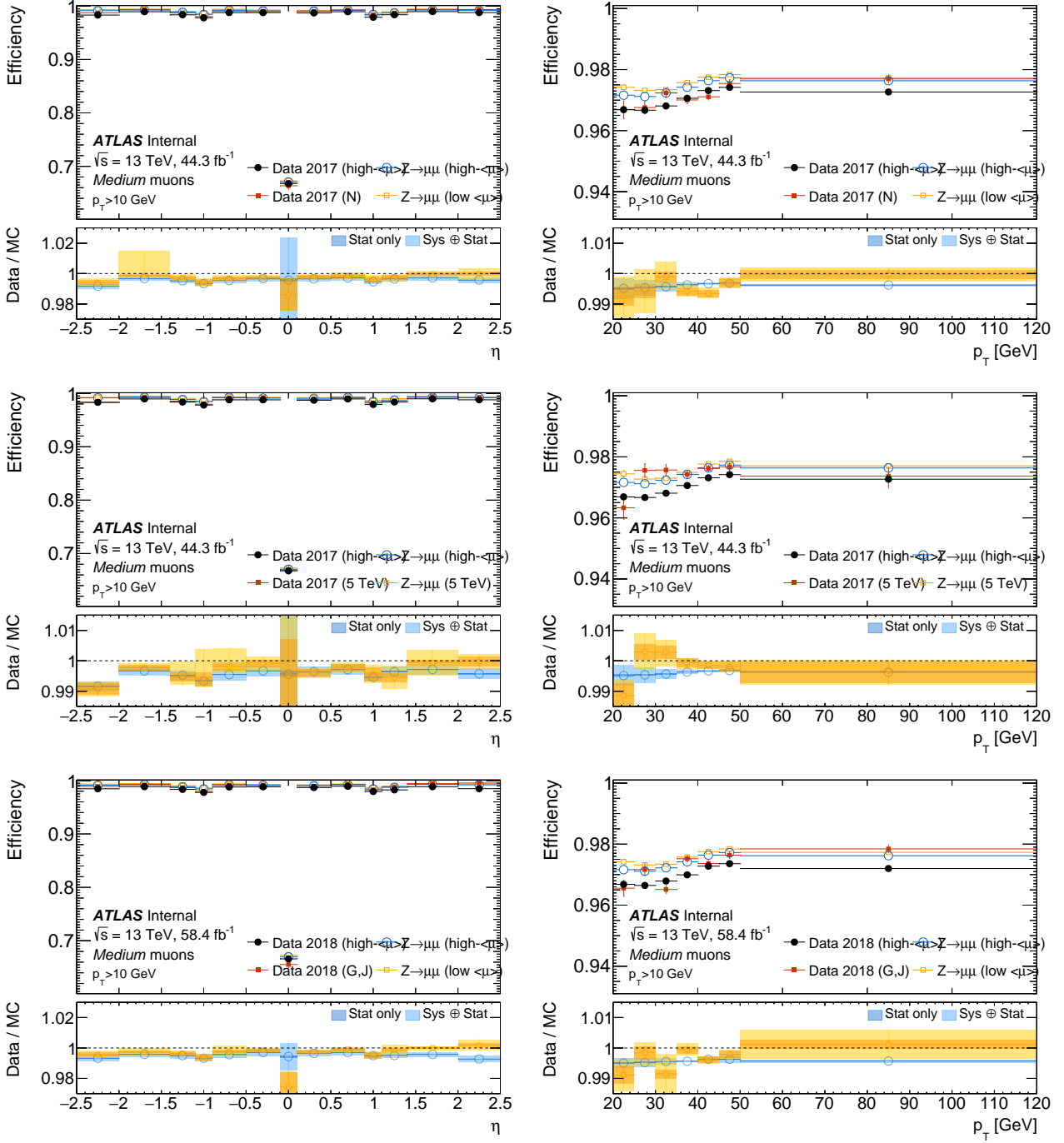


Figure 121: Comparison of reconstruction efficiencies for Medium muons using the low- μ runs of 2017 and 2018 at a centre-of-mass energy of $\sqrt{s} = 13$ TeV and $\sqrt{s} = 5$ TeV. Efficiencies are shown as a function of muon η, p_T . Red (orange) points correspond to low- μ data (MC), while the black (blue) points are high- μ data (MC). The bottom panels show the data/MC ratio for the low- μ (orange) and high- μ (blue) sets with statistical and total uncertainties.

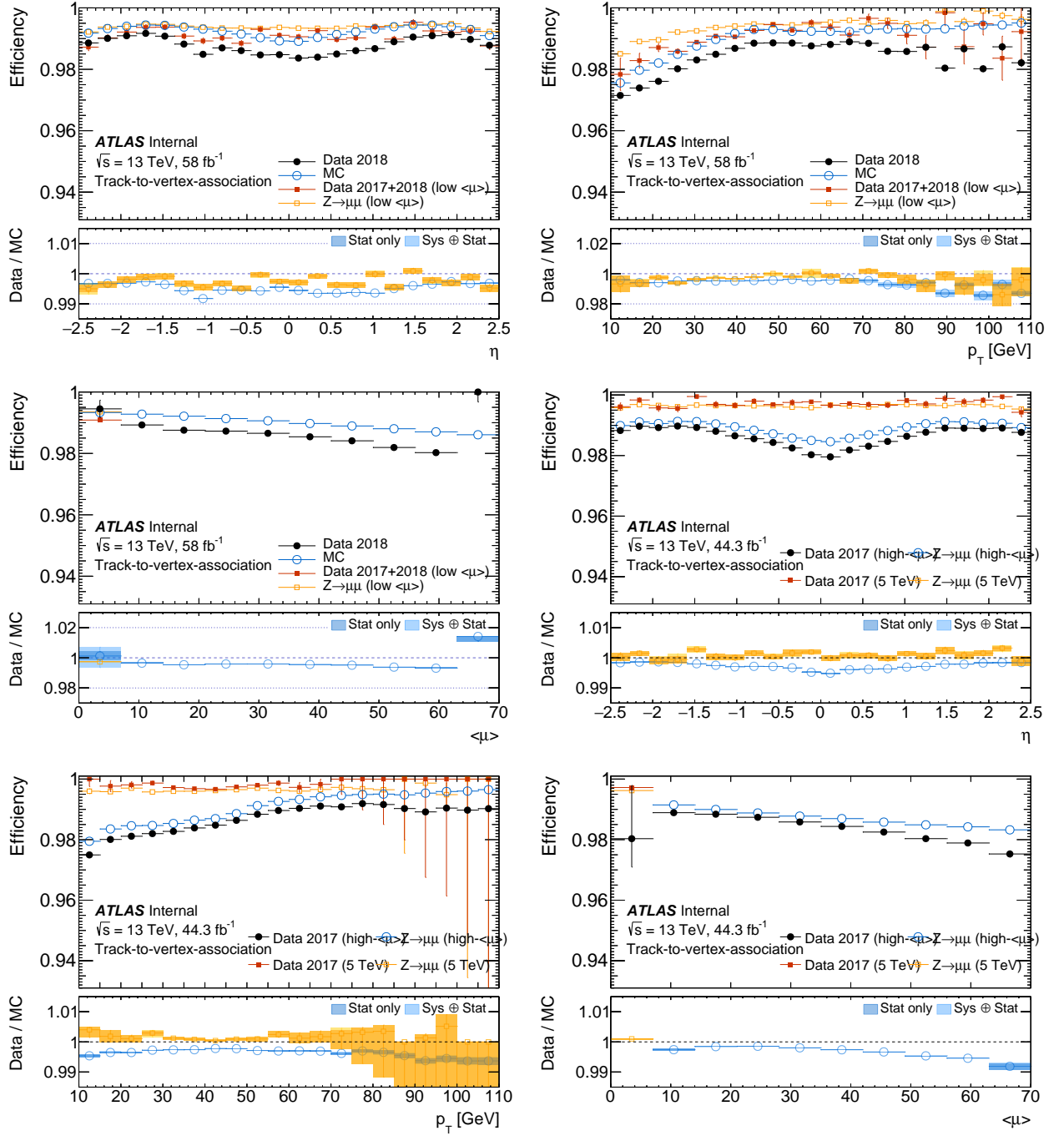


Figure 122: Comparison of TTVA efficiencies for Medium muons using the low- μ runs of 2017+18 at $\sqrt{s} = 13$ TeV (top row) and low- μ runs of 2017 at $\sqrt{s} = 5$ TeV (lower row). The low- μ results compared to a high- μ data set as specified in the plot legend. Efficiencies are shown as function of muon η (left) and p_T (middle) and the mean number of interactions $\langle \mu \rangle$ (right). Red (orange) points correspond to low- μ data (MC), while the black (blue) points are high- μ data (MC). The bottom panels show the data/MC ratio for the low- μ (orange) and high- μ (blue) sets with statistical and total uncertainties.

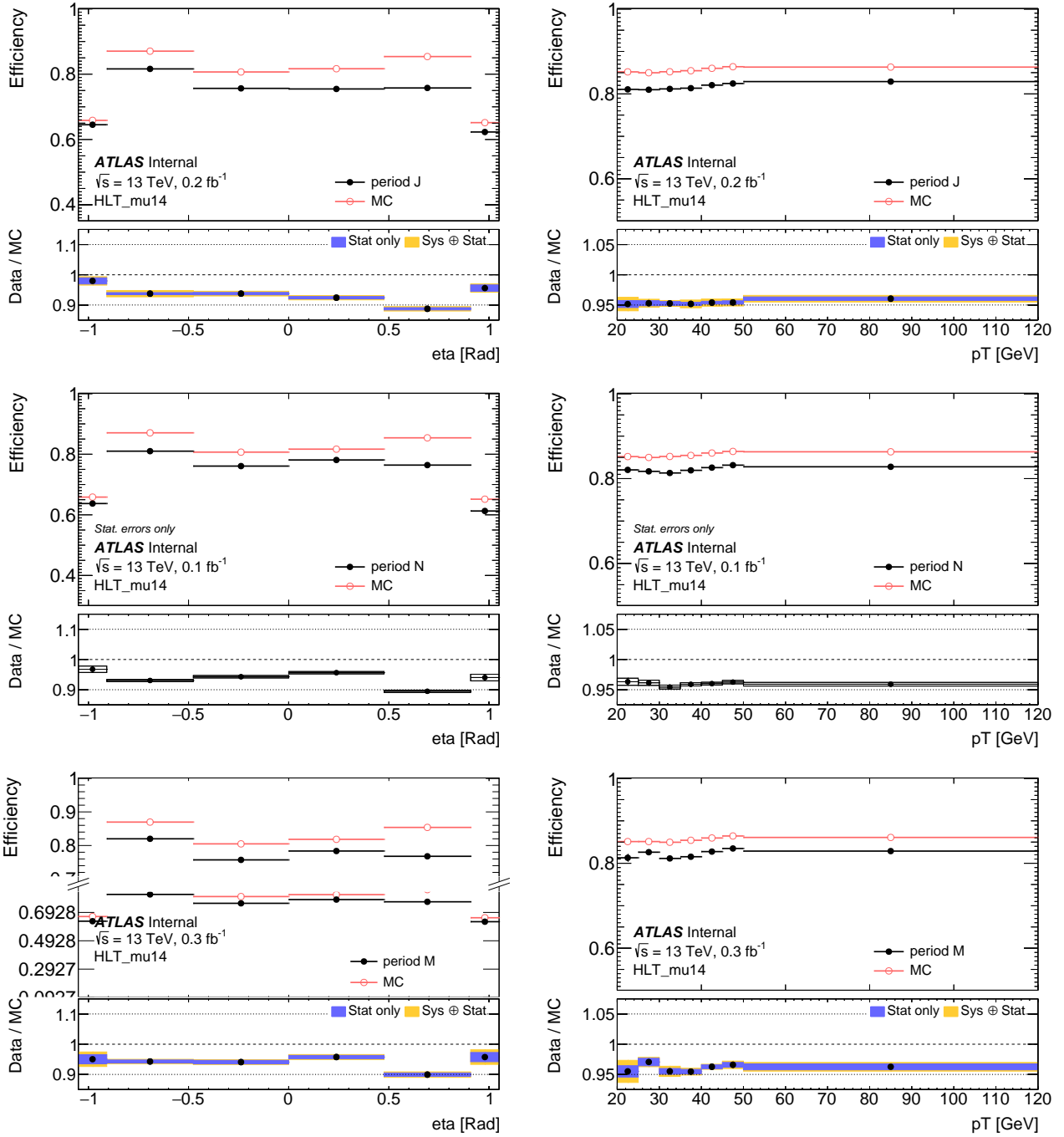


Figure 123: 1D trigger efficiency and systematic uncertainty in data and MC, 5 and 13 TeV from 2017 and 2018 for probes from the eta barrel region and inclusive ϕ , p_T distributions. Trigger sectors in the barrel and endcap regions are different, only the barrel trigger is shown here. The bin edges correspond to physical edges of the trigger sectors.

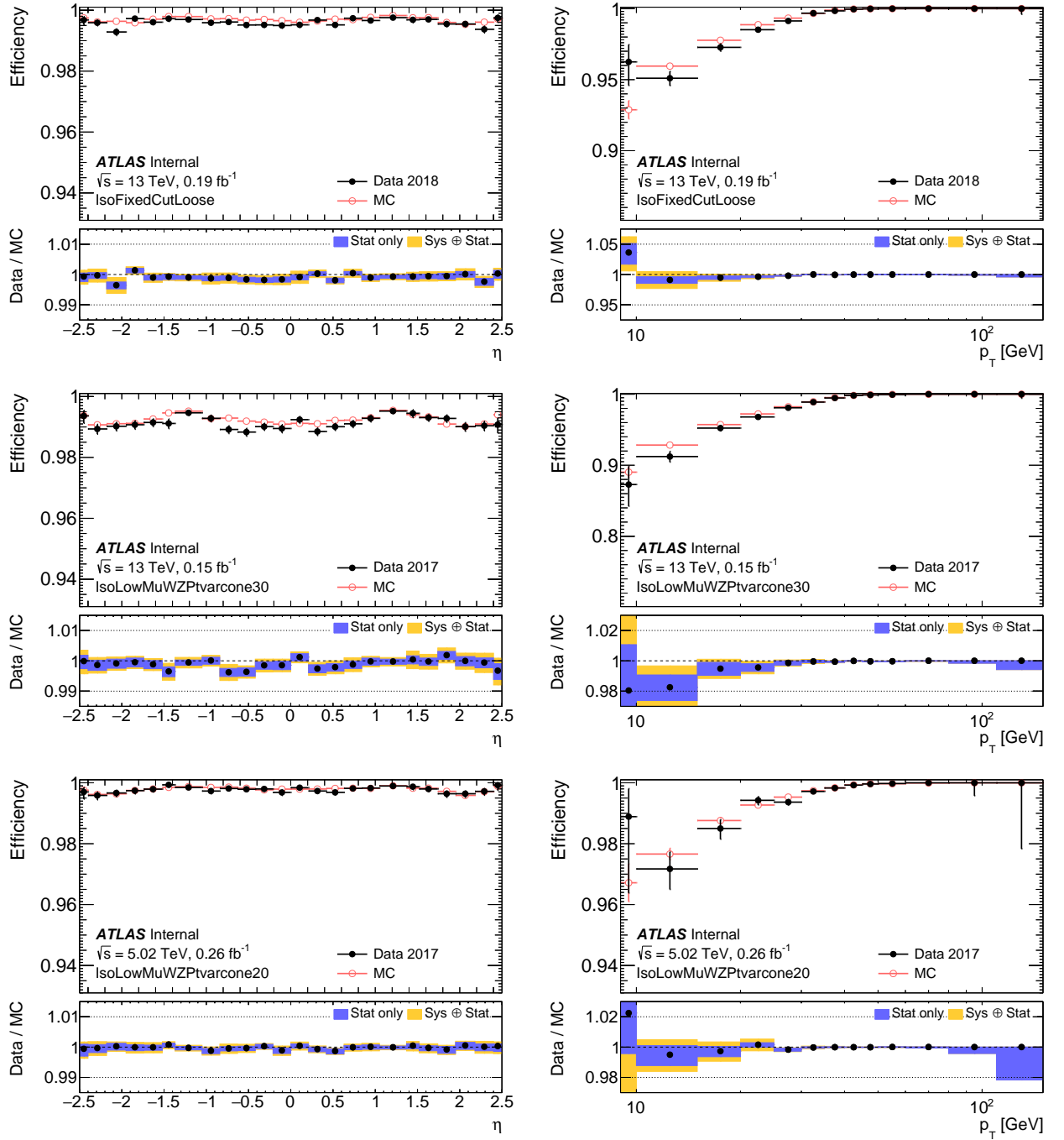


Figure 124: Efficiencies for Ptvarcone20 isolation selections measured in 2017 and 2018 data and MC 13 TeV and 5 TeV as a function of muon η (left) and p_T (right). The bottom panels show the data/MC scale factors with statistical uncertainties represented by blue boxes, while a sum in quadrature of statistical and systematic uncertainties is represented by orange boxes.

1.3 Hadronic recoil calibration

The study of the W boson kinematics by its leptonic decay products $W^\pm \rightarrow l^\pm \nu$ is complicated first of all due to the escaping neutrino that carries away substantial information. However, the W boson transverse momentum can still be measured. As it was shown in Chapter 5, the largest part of the W boson p_T is coming from the initial state radiation. The energy of the created parton shower can be measured:

$$\vec{p}_T^V = \vec{p}_T^\ell + \vec{p}_T^\nu = - \sum_{i=\text{ISR } q,g} \vec{p}_{Ti} = -\vec{u}_T, \quad (1.4)$$

where \vec{p}_T^V , \vec{p}_T^ℓ and \vec{p}_T^ν are the transverse momenta of the vector boson, lepton and neutrino respectively. The vector sum of all the partons from the ISR is called the *hadronic recoil*: $\sum_{i=\text{ISR } q,g} \vec{p}_{Ti} = \vec{u}_T$. Then the missing transverse momentum $E_T^{\vec{\text{miss}}}$ of the escaping neutrino can be measured as:

$$E_T^{\vec{\text{miss}}} = \vec{p}_T^\nu = -(\vec{u}_T + \vec{p}_T^\ell). \quad (1.5)$$

The Hadronic Recoil (HR) reconstruction uses the Particle Flow Objects (PFO), which were defined and described in Section ???. It is important to exclude lepton(s) from the HR of a W(Z) event to avoid double counting. A cone of $\Delta R < 0.2$ is removed around the lepton(s) and is replaced by the same-size cone in the same η and ϕ region, but $\Delta R > 0.4$ away from any lepton. Only the leptons above $p_T > 10\text{GeV}$ and passing fiducial cuts in η and ID requirements are removed from the HR.

Another important quantity for the HR is the $\sum E_T$ - a scalar sum of the transverse energies of all the PFO. The $\sum E_T$ represents the total event activity, there is a relation between the $\sum E_T$ magnitude and u_T resolution. The underlying event activity, pile-up and soft emissions can be characterized by introducing another quantity: $\Sigma \vec{E}_T = \Sigma E_T - u_T$, which has the meaning of ΣE_T with hard activity subtracted.

For the calibration of the HR it is better to introduce quantities that are defined in a natural physical way. The vector boson transverse momentum provides a natural axis which is convenient to use for the 2-component decomposition of the u_T vector. The u_T component parallel to the vector boson p_T :

$$u_{\parallel} = \frac{\vec{p}_T^V \cdot \vec{u}_T}{p_T^V}, \quad (1.6)$$

and a perpendicular component:

$$u_{\perp} = \frac{|\vec{p}_T^V \times \vec{u}_T|}{p_T^V}. \quad (1.7)$$

Ideally we would like to have $u_{\parallel} = 1$ and $u_{\perp} = 0$, but due to detector effects it is never the case. The perpendicular component u_{\perp} can be thought of as the HR resolution, while u_{\parallel} has a physical meaning of the recoil scale. Another important quantity is called the *bias*:

$$b = u_{\parallel} + p_T^V, \quad (1.8)$$

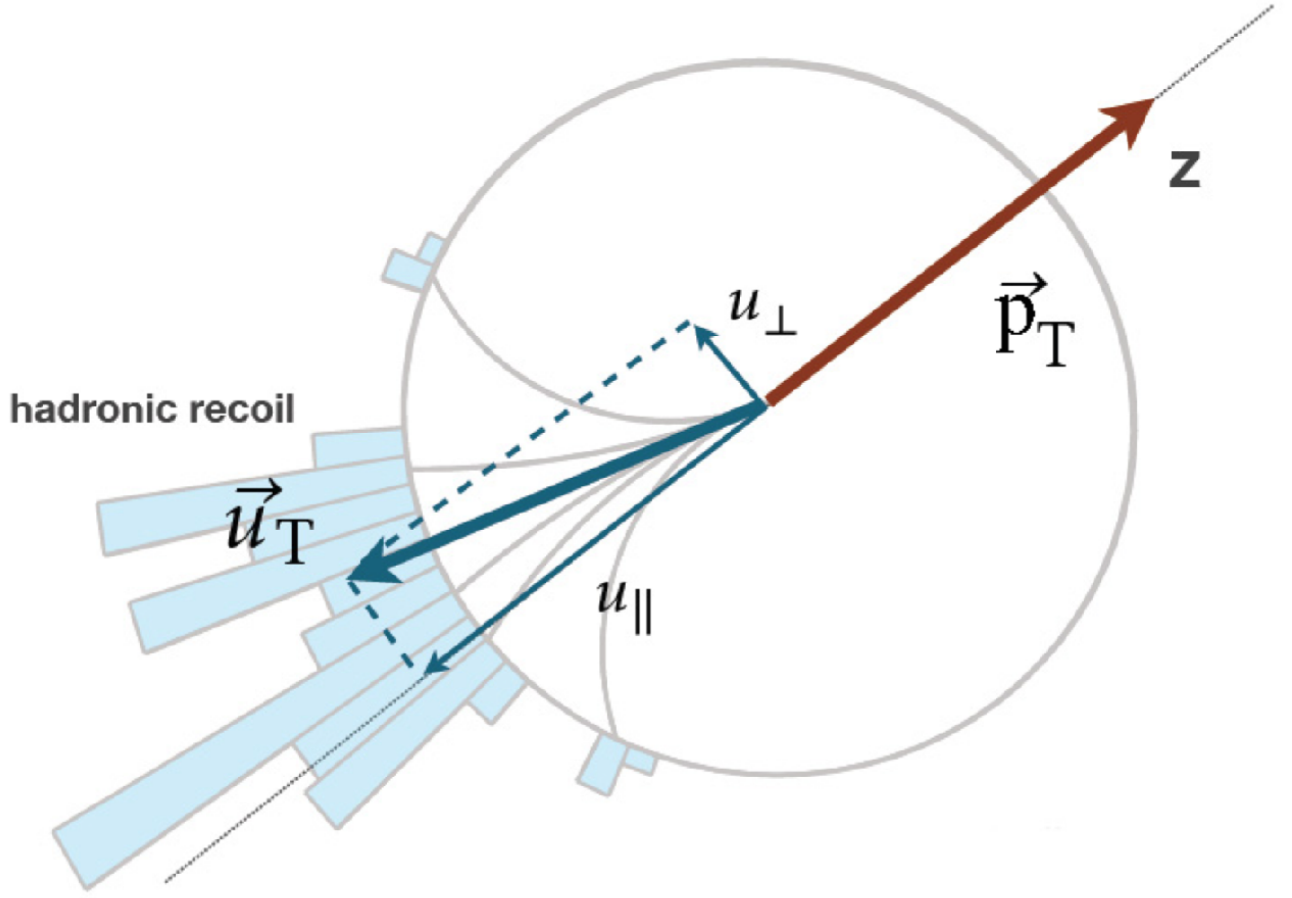


Figure 125: The hadronic recoil vector in the transverse plane and its components with respect to vector boson p_T .

which is expected to be centered around zero. In data, of course, we don't know the p_T^V of the truth boson. However, in Z decay events we can use the dilepton transverse momentum $p_T^{\ell\ell}$ as an axis for u_{\perp} and u_{\parallel} decomposition - considering the u_T resolution the difference between p_T^V and $p_T^{\ell\ell}$ is negligible. In W data events it is only possible to use p_T^l for u_T decomposition.

1.3.1 SET and u_T reweighting

Despite the fact that the two electroweak bosons, W and Z, share lot of similarities, there are also small but notable differences in valence quark content and PDFs, energy scale, etc. This leads to differences in underlying event and p_T^V spectra, which manifest themselves in the observables like ΣE_T , $\Sigma \bar{E}_T$, u_T . For the high-precision measurements it is important to ensure that these quantities as well as their correlations are modelled properly. It is also important to match these correlations in data and MC simulations. Figure 126 demonstrates that the baseline POWHEGMC simulations lead to a significant mismodelling of the $\Sigma \bar{E}_T - p_T^V$ correlation, while SHERPA shows much better agreement with the data

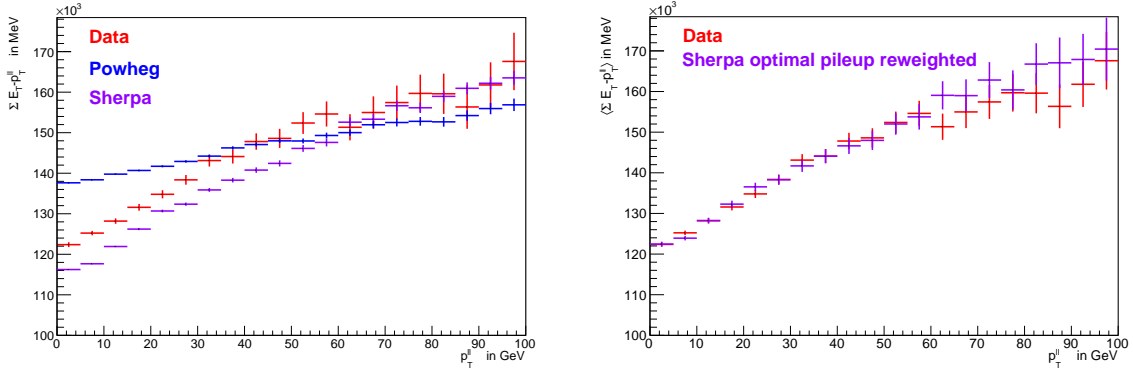


Figure 126: Comparison of the $\Sigma E_T - p_T^{\ell\ell}$ description in data of the two MC samples PowHEG and SHERPA at 13 TeV, showing $\Sigma E_T - p_T^{\ell\ell}$ inclusively (left). Figure on the right shows the comparison of SHERPA to the data after a dedicated pileup reweighting.

from the very beginning. After applying a special pile-up reweighting of SHERPA samples a very good agreement with the data is achieved.

In order to obtain proper distributions in the MC samples, a three-step reweighting procedure is implemented.

First weight is obtained by from the 2D $\Sigma \vec{E}_T - p_T^V$ distributions ratio in Data and MC:

$$w_{2D}^Z(\Sigma \vec{E}_T, p_T^{\ell\ell}) = \frac{h^{\text{data}, Z}(\Sigma \vec{E}_T, p_T^{\ell\ell})}{h^{\text{MC}, Z}(\Sigma \vec{E}_T, p_T^{\ell\ell})}, \quad (1.9)$$

where the following binning is used:

- $p_T^{\ell\ell}$ (13 TeV) = [0, 2, 3, 4, 5, 6, 7, 8, 9, 10, 12, 16, 20, 25, 30, 40, 50, 55, 65, 80, 100, 200, ∞] GeV
- $p_T^{\ell\ell}$ (5 TeV) = [0, 2, 3, 4, 5, 6, 7, 8, 9, 10, 12, 16, 20, 25, 27, 30, 40, 45, 50, 60, 70, 100, 200, ∞] GeV
- $\Sigma \vec{E}_T$ (13 TeV) = [0, 10, 20, 30, ..., 380, ∞] GeV
- $\Sigma \vec{E}_T$ (5 TeV) = [0, 10, 20, 30, ..., 280, ∞] GeV

This reweighting is obtained from the $Z \rightarrow \mu\mu$ events for 5 and 13 TeV datasets and applied to both W and Z Monte-Carlo samples. In W events the p_T^V is used instead of $p_T^{\ell\ell}$ for obvious reasons. This reweighting assures very good agreement for the Z events, but perfect agreement is not guaranteed for the W events. For this reason a second reweighting is derived from the data: $\Sigma \vec{E}_T$ weight is extracted in bins of u_T of 4 GeV width and applied to W MC events on top of the first 2D reweighting:

$$w_{j, \text{sliced}}^{W^\pm}(\Sigma \vec{E}_T) = \frac{h_j^{\text{data}, W^\pm}(\Sigma \vec{E}_T)}{h_j^{\text{MC}, W^\pm, Z2D\text{mod}}(\Sigma \vec{E}_T)}, \quad (1.10)$$

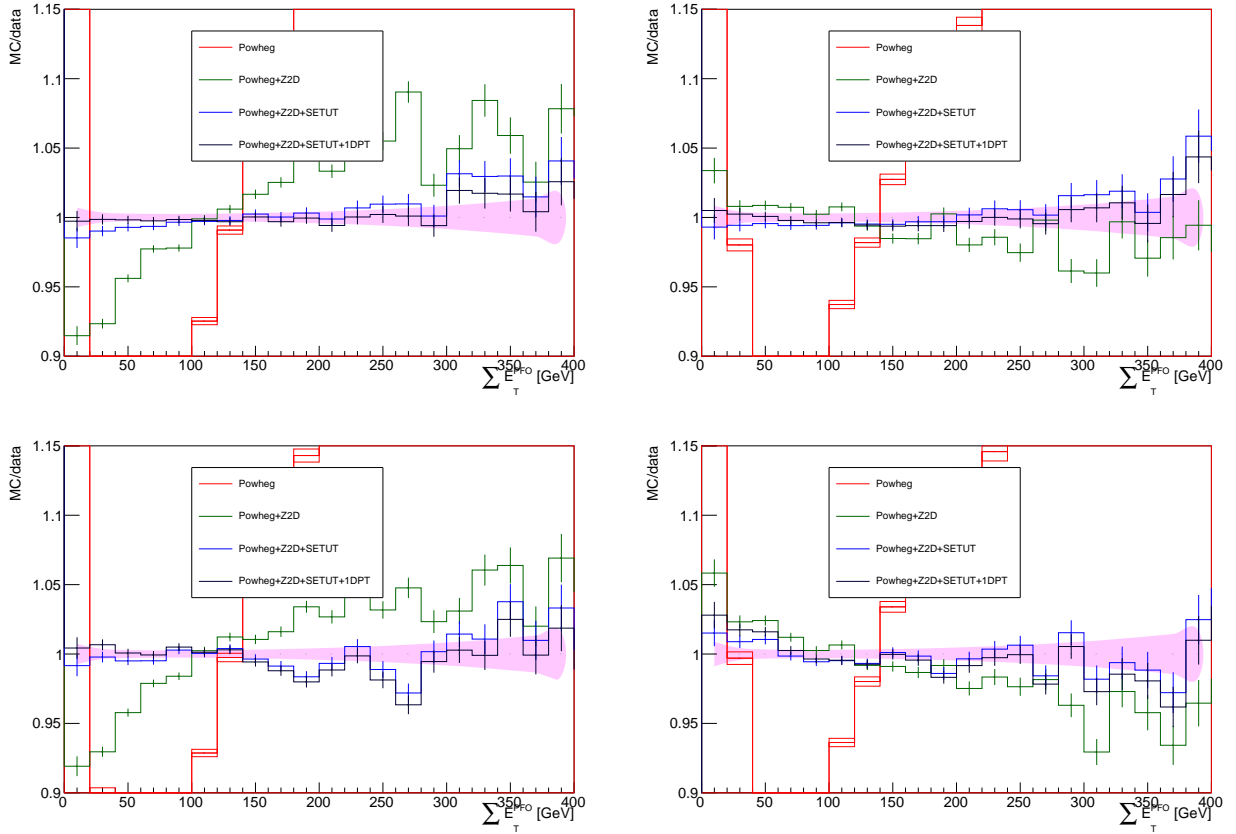


Figure 127: Ratio of data to predictions in $W \rightarrow \mu\nu$ events at 13 TeV for the $\Sigma \vec{E}_T$ distribution, before and after each $\Sigma \vec{E}_T$ modeling reweighting step. The color band is the data statistical uncertainty. The prediction uncertainty only includes the statistical uncertainty. 'Powheg' uses the baseline MC for the signal. 'Powheg+Z2D' has the 2D $(\Sigma \vec{E}_T, p_T^{true,V})$, Z-based reweighting applied. 'Powheg+Z2D+SETUT' adds the $\Sigma \vec{E}_T$ reweighting in bins of u_T . 'Powheg+Z2D+SETUT+1DPT' adds the 1D reweighting to recover the initial $p_T^{true,V}$ spectrum.

where h_j stands for the normalized $\Sigma \vec{E}_T$ distribution in the u_T bin number j after the standard selection. This reweighting improves the $\Sigma \vec{E}_T$ modelling, but distorts the p_T^V spectrum. This motivates the third correction reweighting with the following weight:

$$w_{1D}^{W^\pm}(p_T^{true,V}) = \frac{h^{MC,W^\pm,mod}(p_T^{true,V})}{h^{MC,W^\pm,orig}(p_T^{true,V})}. \quad (1.11)$$

The $h^{MC,W^\pm,orig}(p_T^{true,V})$ stands for the original $p_T^{true,V}$ spectrum before any reweightings were applied. The total weight applied to an event is the product of the three weights described above: $w_{2D}^Z(\Sigma \vec{E}_T, p_T^{true,V}) \times w_{j,sliced}^{W^\pm}(\Sigma \vec{E}_T) \times w_{1D}^{W^\pm}(p_T^{true,V})$. The results on the reweighting are shown in Figures 127 and 128 for 13 and 5 TeV respectively.

The closure of the procedure is checked with SHERPAMC simulation used as pseudo-data, as we

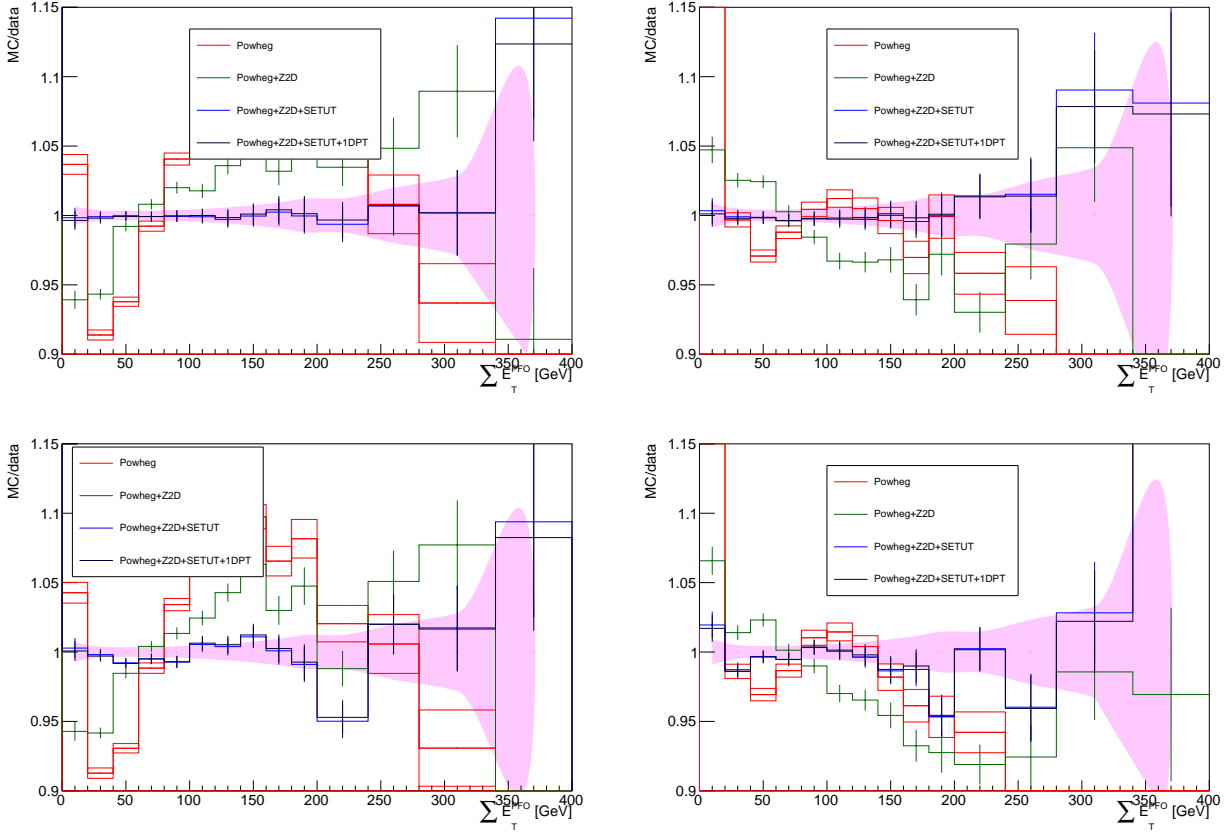


Figure 128: Ratio of data to predictions in $W \rightarrow \mu\nu$ events at 5 TeV for the $\Sigma \vec{E}_T$ distribution, before and after each $\Sigma \vec{E}_T$ modeling reweighting step. The color band is the data statistical uncertainty. The prediction uncertainty only includes the statistical uncertainty. 'Powheg' uses the baseline MC for the signal. 'Powheg+Z2D' has the 2D $(\Sigma \vec{E}_T, p_T^{true,V})$, Z-based reweighting applied. 'Powheg+Z2D+SETUT' adds the $\Sigma \vec{E}_T$ reweighting in bins of u_T . 'Powheg+Z2D+SETUT+1DPT' adds the 1D reweighting to recover the initial $p_T^{true,V}$ spectrum.

don't have the p_T^V distribution from the data. The residual non-closure of less than 1% is treated as a systematic uncertainty.

1.3.2 u_X and u_Y correction

Azimuthal angle distribution is another discrepancy between the MC simulation and the data. While the simulated events have a flat ϕ distribution, the data events show a non-uniform distribution which is probably caused by detector imperfections or ageing. The correction is performed by introducing additive corrections to the u_X and u_Y components of the HR. The corrections are derived as a mean difference between the data and MC as a function of $\Sigma \vec{E}_T$:

$$\begin{aligned} u_X^{\text{MC,corr}} &= u_X^{\text{MC}} + [(\langle u_X^{\text{data}} \rangle - \langle u_X^{\text{MC}} \rangle)(\Sigma \vec{E}_T)] \\ u_Y^{\text{MC,corr}} &= u_Y^{\text{MC}} + [(\langle u_Y^{\text{data}} \rangle - \langle u_Y^{\text{MC}} \rangle)(\Sigma \vec{E}_T)] \end{aligned} \quad (1.12)$$

The dependence of the mean differences $\langle u_X^{\text{data}} \rangle - \langle u_X^{\text{MC}} \rangle$ and $\langle u_Y^{\text{data}} \rangle - \langle u_Y^{\text{MC}} \rangle$ on $\Sigma \bar{E}_T$ is fitted with a linear function. The corrected ϕ distributions are shown in Figure 129. It was shown that the correlation between the correction and the magnitude of the recoil is weak and the effect of the correction on the measured W spectrum is of per mille level. For this reason no uncertainty was assigned to this correction.

1.3.3 Resolution and response corrections

The correction function for $\sigma(u_\perp)(\Sigma \bar{E}_T, p_T^{\ell\ell})$ is constructed in bins of $p_T^{\ell\ell}$ in the following way:

$$r(\Sigma \bar{E}_T, p_T^{\ell\ell}) = \frac{\sigma(u_\perp)^{\text{data}}}{\sigma(u_\perp)^{\text{MC}}}, \quad (1.13)$$

where both $\sigma(u_\perp)$ functions are obtained as a linear fit to $\sqrt{\Sigma \bar{E}_T}$:

$$\sigma(u_\perp)(\Sigma \bar{E}_T) = c + d \cdot \sqrt{\Sigma \bar{E}_T}. \quad (1.14)$$

with the following $p_T^{\ell\ell}$ binning:

- 5 TeV: $p_T^{\ell\ell} = [0, 3, 4, 6, 7, 9, 11, 13, 16, 20, 26, 40, \infty]$ GeV
- 13 TeV: $p_T^{\ell\ell} = [0, 3, 4, 6, 7, 9, 10, 12, 14, 17, 21, 26, 33, 49, \infty]$ GeV

Then the correction for the W boson events is performed using the ratio function as a factor:

$$u_\perp^{\text{MC,corr}} = u_\perp^{\text{MC}} \times r(\Sigma \bar{E}_T, p_T^{\text{true},V}). \quad (1.15)$$

The correction of the parallel component u_\parallel is done as follows:

$$u_\parallel^{\text{MC,corr}} = \langle u_\parallel^{\text{data}} \rangle + (\langle b^{\text{data}} \rangle - \langle b^{\text{MC}} \rangle) \cdot r_\parallel + (u_\parallel^{\text{MC}} - \langle u_\parallel^{\text{data}} \rangle) \cdot r_\parallel. \quad (1.16)$$

Here the resolution correction factor r_\parallel is in equation 1.13, but reads as $\sigma(u_\parallel)^{\text{data}}/\sigma(u_\parallel)^{\text{MC}}$.

The average $\langle u_\parallel^{\text{data}} \rangle$ assumes averaging over all data events in bins of $p_T^{\ell\ell}$ and $\Sigma \bar{E}_T$. The $\Sigma \bar{E}_T$ bins are 10 GeV wide for 5 TeV and 20 GeV wide for 13 TeV. The in each $\Sigma \bar{E}_T$ bin the $p_T^{\ell\ell}$ dependence is fitted with a linear function:

$$\langle u_\parallel^{\text{data}} \rangle(p_T^{\ell\ell}) = e + f \cdot p_T^{\ell\ell}. \quad (1.17)$$

Similarly the difference of the biases $(\langle b^{\text{data}} \rangle - \langle b^{\text{MC}} \rangle)$ is computed in the same bins of $p_T^{\ell\ell}$ and $\Sigma \bar{E}_T$ and fitted in each $\Sigma \bar{E}_T$ bin with a linear function of $p_T^{\ell\ell}$.

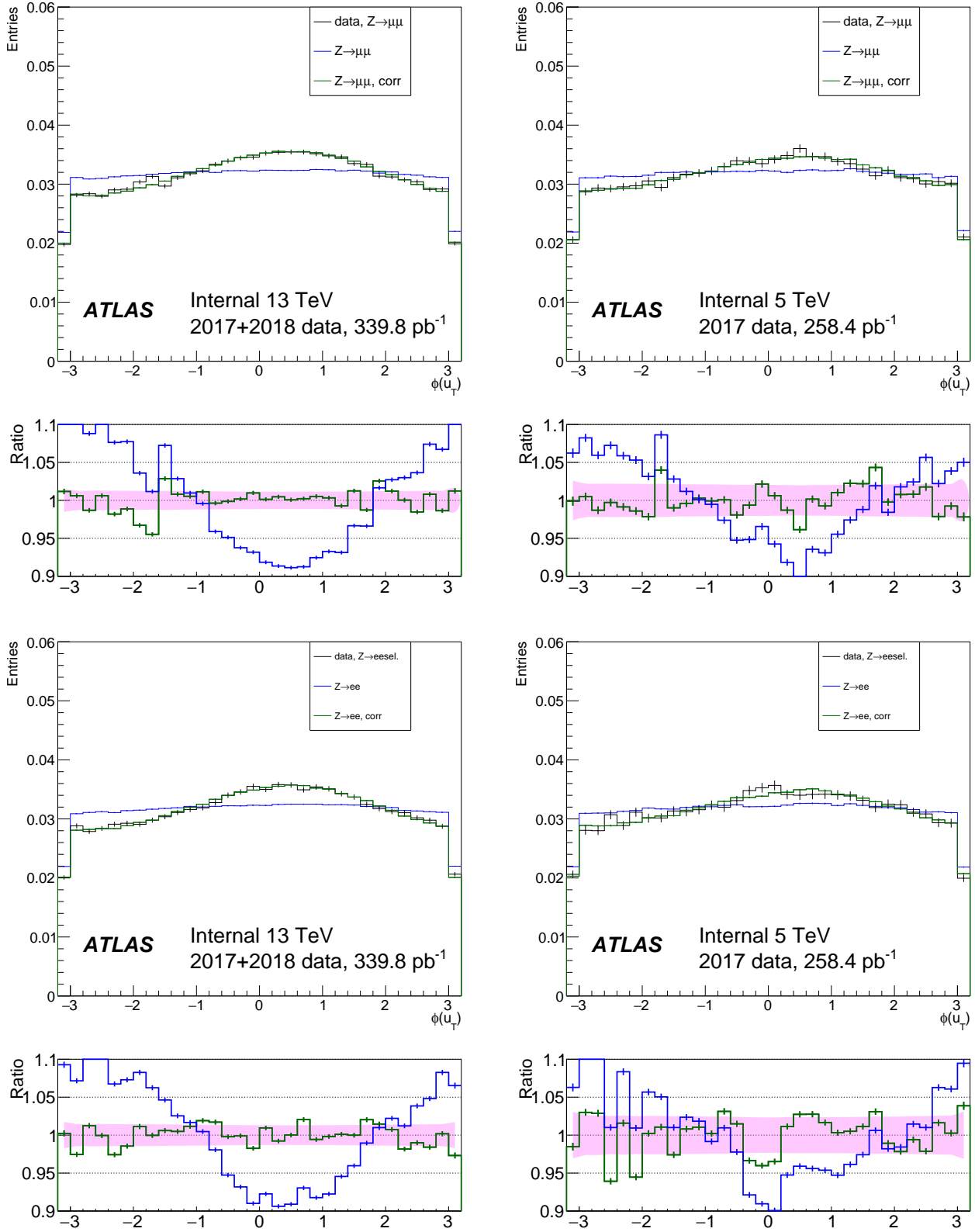


Figure 129: $\phi(u_T)$ at 5 and 13 TeV, for the data and the simulation before and after u_X and u_Y correction, in Z events. The band in the ratio panel is the data statistical uncertainty.

1.4 Angular coefficients correction

The fully differential cross-section of the fully leptonic Drell-Yan process can be factorized in the following way [11]:

$$\frac{d\sigma}{dp_1 dp_2} = \left[\frac{d\sigma(m)}{dm} \right] \left[\frac{d\sigma(y)}{dy} \right] \left[\frac{d\sigma(p_T, y)}{dp_T dy} \left(\frac{d\sigma}{dy} \right)^{-1} \right] \left[(1 + \cos^2 \theta + \sum_{i=0}^7 A_i(p_T, y) P_i(\cos \theta, \phi)) \right], \quad (1.18)$$

where p_1 and p_2 are the 4-momenta of the two leptonic decay products; m , p_T and y are the dilepton system invariant mass, transverse momentum and rapidity respectively; θ is the polar and ϕ is azimuthal coordinates of the lepton (e^- in $W^- \rightarrow e^- \nu$ or ν in $W^+ \rightarrow e^+ \nu$). The angular dependence is decomposed in seven spherical harmonics P_i with numerical coefficients A_i . The numerical coefficients A_i are in general case are a function of p_T , y and m , but the mass dependence may be neglected [12]. The A_i coefficients were derived to the NNLO precision using the DYNNLO program for fixed-order cross-section calculations [13].

The default MC samples generated by POWHEG+PYTHIA8 were reweighted at the event level in order to introduce the corrections:

$$w(\cos \theta, \phi, p_T, y) = \frac{1 + \cos^2 \theta + \sum_i A'_i(p_T, y) P_i(\cos \theta, \phi)}{1 + \cos^2 \theta + \sum_i A_i(p_T, y) P_i(\cos \theta, \phi)}, \quad (1.19)$$

where $A_i(p_T, y)$ are the angular coefficients, predicted by the POWHEG+PYTHIA8 simulation and $A'_i(p_T, y)$ are the NNLO coefficients evaluated at $O(\alpha^2)$ precision.

422 Bibliography

- 423 [1] Jan Kretzschmar. *Samples and Physics modelling for low pile-up runs taken in 2017 and 2018*.
 424 Tech. rep. ATL-COM-PHYS-2019-075. Geneva: CERN, Feb. 2019. URL: [https://cds.cern.ch/](https://cds.cern.ch/record/2657141)
 425 [record/2657141](https://cds.cern.ch/record/2657141).
- 426 [2] Morad Aaboud et al. “Electron and photon energy calibration with the ATLAS detector using
 427 2015–2016 LHC proton-proton collision data”. In: *JINST* 14.03 (2019), P03017. DOI: 10.1088/
 428 1748-0221/14/03/P03017. arXiv: 1812.03848 [hep-ex].
- 429 [3] ATLAS Collaboration. “Electron and photon energy calibration with the ATLAS detector using
 430 2015–2016 LHC proton-proton collision data”. In: *JINST* 14 (2019), P03017. DOI: 10.1088/1748-
 431 0221/14/03/P03017. arXiv: 1812.03848 [hep-ex].
- 432 [4] “Electron and photon performance measurements with the ATLAS detector using the 2015-2017
 433 LHC proton-proton collision data”. In: *JINST* 14. arXiv:1908.00005. 12 (Aug. 2019). 31 figures,
 434 3 tables. All figures including auxiliary figures are available at [https://atlas.web.cern.ch/At-](https://atlas.web.cern.ch/Atlas/GROUPS/PHYSICS/PAPERS/EGAM-2018-01)
 435 [las/GROUPS/PHYSICS/PAPERS/EGAM-2018-01](https://atlas.web.cern.ch/Atlas/GROUPS/PHYSICS/PAPERS/EGAM-2018-01), P12006. 70 p. DOI: 10.1088/1748-0221/14/
 436 12/P12006. URL: <https://cds.cern.ch/record/2684552>.
- 437 [5] ATLAS Collaboration. “Electron and photon energy calibration with the ATLAS detector using
 438 LHC Run 1 data”. In: *Eur. Phys. J. C* 74 (2014), p. 3071. DOI: 10.1140/epjc/s10052-014-3071-4.
 439 arXiv: 1407.5063 [hep-ex].
- 440 [6] Nansi Andari et al. *Electron and photon energy calibration with the ATLAS detector using 2015-2017*
 441 *LHC proton-proton collision data*. Tech. rep. ATL-COM-PHYS-2018-1720. Geneva: CERN, 2018.
 442 URL: <https://cds.cern.ch/record/2651890>.
- 443 [7] Morad Aaboud et al. “Electron reconstruction and identification in the ATLAS experiment using
 444 the 2015 and 2016 LHC proton-proton collision data at $\sqrt{s} = 13$ TeV”. In: *Eur. Phys. J. C* 79.8
 445 (2019), p. 639. DOI: 10.1140/epjc/s10052-019-7140-6. arXiv: 1902.04655 [physics.ins-
 446 det].
- 447 [8] Georges Aad et al. “Electron and photon performance measurements with the ATLAS detector
 448 using the 2015–2017 LHC proton-proton collision data”. In: *JINST* 14.12 (2019), P12006. DOI:
 449 10.1088/1748-0221/14/12/P12006. arXiv: 1908.00005 [hep-ex].
- 450 [9] *Study of alignment-related systematic effects on the ATLAS Inner Detector tracking*. Tech. rep. ATLAS-
 451 CONF-2012-141. Geneva: CERN, Oct. 2012. URL: <https://cds.cern.ch/record/1483518>.
- 452 [10] Nicolas Maximilian Koehler et al. *Muon Efficiency Measurements on the Full Run 2 dataset*. Tech.
 453 rep. ATL-COM-PHYS-2019-176. Geneva: CERN, Mar. 2019. URL: [https://cds.cern.ch/](https://cds.cern.ch/record/2665704)
 454 [record/2665704](https://cds.cern.ch/record/2665704).
- 455 [11] Sidney D. Drell and Tung-Mow Yan. “Massive Lepton-Pair Production in Hadron-Hadron Col-
 456 lisions at High Energies”. In: *Phys. Rev. Lett.* 25 (5 Aug. 1970), pp. 316–320. DOI: 10.1103/
 457 PhysRevLett.25.316. URL: <https://link.aps.org/doi/10.1103/PhysRevLett.25.316>.

- 458 [12] E. Mirkes. “Angular decay distribution of leptons from W-bosons at NLO in hadronic collisions”.
 459 In: *Nuclear Physics B* 387.1 (1992), pp. 3–85. issn: 0550-3213. doi: [https://doi.org/10.1016/](https://doi.org/10.1016/0550-3213(92)90046-E)
 460 0550-3213(92)90046-E. url: [http://www.sciencedirect.com/science/article/pii/](http://www.sciencedirect.com/science/article/pii/055032139290046E)
 461 055032139290046E.
- 462 [13] Stefano Catani et al. “Vector Boson Production at Hadron Colliders: A Fully Exclusive QCD
 463 Calculation at Next-to-Next-to-Leading Order”. In: *Phys. Rev. Lett.* 103 (8 Aug. 2009), p. 082001.
 464 doi: 10.1103/PhysRevLett.103.082001. url: [https://link.aps.org/doi/10.1103/](https://link.aps.org/doi/10.1103/PhysRevLett.103.082001)
 465 PhysRevLett.103.082001.